Spring 5-15-2020

Nucleation Dynamics for Water Condensation on Hydrophobic Surfaces in the Presence of Non-Condensable Gases

Xinyu Jiang
Washington University in St. Louis

Washington University in St. Louis

McKelvey School of Engineering

Department of Department Name

Thesis Examination Committee:

Patricia Weisensee, Chair

David Peters

Ramesh Agarwal

Nucleation Dynamics for Water Condensation on Hydrophobic Surfaces in the Presence of Non-Condensable Gases

By

Xinyu Jiang

A thesis presented to the McKelvey School of Engineering of Washington University in St. Louis in partial fulfillment of the requirements for the degree of Master of Science

May 2020

St. Louis, Missouri

Dedication

I would like to dedicate this thesis to my father (Zhong Jiang) and my mother (Jiarong Fu) for their unconditional support.

I will never succeed without their guidance, influence and encouragement.

Acknowledgments

I would like to express my deepest gratitude to those who helped me during my research in thermal fluids lab at Washington University in St. Louis.

My deepest gratitude goes first and foremost to Professor Patricia Weisensee for her encouragement and guidance throughout my research. Her knowledge, experience and guidance has helped me to accomplish my entire research and thesis in reasonable steps. Without her I won't have the opportunity to explore the academic world of dropwise condensation.

Second, I would like to express my heartfelt gratitude to Jianxing Sun and Junhui Li for all the effort they put in to help me. The experienced idea about how to make researches of Jianxing Sun helped me to start my research smoothly. And the careful guidance of Junhui Li who helped me to have the ability to conduct my research.

Finally, I would like to thank all the teachers, all the group members in thermal fluids lab. It is the harmonious communication environment and exchanging of different ideas that let me keep learning and progress.

Xinyu Jiang

Washington University in St. Louis

April 2020

Table of Contents

List of Figures

List of Tables

Abstract

Nucleation Dynamics for Water Condensation on Hydrophobic Surfaces in the Presence of Non-Condensable Gases

by

Xinyu Jiang

Master of Science in Mechanical Engineering

Washington University in St. Louis, 2020

Research Advisor: Professor Patricia Weisensee

The density and rate of nucleation (here-in called nucleation density rate) significantly influences the heat transfer performance during dropwise condensation, as more than 70% of the total heat transfer happen for droplets smaller than 10 μm. Based on the classical nucleation theory, supersaturation strongly influences nucleation dynamics. However, the presence of non-condensable gas can strongly reduce the nucleation density rate by forming a vapor-depleted gas diffusion layer. Therefore, this work studied the relationship between nucleation density rate and supersaturation ratio during dropwise condensation on subcooled smooth hydrophobic surfaces with the presence of non-condensable gases in a custom-built condensation chamber. High-speed imaging and high-resolution microscopy enabled the experimental quantification of condensation dynamics. These were then compared to theoretical values based on the classical nucleation density. Based on the present experiments and a size distribution model, the relationship between heat transfer rate and supersaturation ratio were analyzed. Finally, through experimental observations, it is shown that the fast movement of relatively larger droplets can disturb the diffusion layer and enhance the nucleation density rate.

Nomenclature

G Gibbs free energy (J)

G_{hom} Gibbs free energy of homogeneous nucleation (J)

G_{het} Gibbs free energy of heterogeneous nucleation (J)

G_v Gibbs free energy per unit volume of the liquid (J/m^3)

V_m molar volume (m^3/mol)

M molar mass (kg/mol)

U internal energy (J)

J nucleation density rate (#/m^{2}s)

T_L system temperature ($^\circ$)

k_B Boltzmann constant (m^{2}kg s^{-2}K^{-1})

p pressure (Pa)

T temperature (K)

S entropy (J/K)

H enthalpy (J)

F_c capillary force (N)

F_g gravity on drop (N)

$n(r)$, $N(r)$ drop size distribution (m^{-3})

r radius (m)

σ surface tension (N/m)

Ψ availability (J)

ρ density (kg/m^3)

r_{min} critical radius for heterogeneous nucleation (m)

r_{max} radius of departure (m)

r_e effective radius (m)

g specific Gibbs free energy (J/kg)

h specific enthalpy (J/kg)

n_l number of liquid molecule

h_{fg} specific latent heat (kJ/kg)

q heat transfer rate (W)

s specific entropy (J/(kg K))

c_p specific heat (J/(kg K))

h_i interfacial heat transfer coefficient (W/(m^2 K))

v specific volume (m^3/kg)

q'' heat flux (W/m^2)

A area (m^2)

R thermal resistance

R_g specific gas constant (J/(kg K))

Greek symbol

δ coating thickness (m)

μ specific chemical potential (J/kg)

τ sweeping period (s)

φ angle ($^\circ$)

θ contact angle ($^\circ$)

λ thermal conductivity (W/(m K))

Subscripts

drop droplet

sub subcooled

max maximum

min minimum

coat coating

cur curvature

hom homogeneous

f difference of area

0 initial condition

v vapor

het heterogeneous

cd conduction

nc non-condensable gas

ct constriction

w wall or surface

s saturated state

l liquid

i interface

Chapter 1: Introduction

Condensation is a very ubiquitous phenomenon in nature, with mainly two types of condensation: filmwise condensation and dropwise condensation. Dropwise condensation generally takes place on non-wetting substrates. This phenomenon was getting more and more attention since Schmidt *et al.* [1] first recognized that the heat transfer coefficient of dropwise condensation from quiescent pure steam can be 5 to 7 times higher than that found in filmwise condensation. Based on this discovery, more and more applications are applied in industry. Brunt *et al* and Poll *et al* used dropwise condensation in a sea water evaporator to gain higher output [2,3]. Although Garatt concluded there is no improvement of output in large evaporator after adding dropwise promoter into the supply steam [4]. Before 1990, industrial application about dropwise condensation didn't have much development as metal surfaces are normally wetted, so they can only form filmwise condensation. What's more, there are no durable promoters that can be used in industrial applications. In 1990, however, Zhao *et al* successfully used sputtering of chromium and nitrogen on copper to improve the quality of dropwise condensation [5-7]. After 2010, dropwise condensation had more industrial applications in different areas, such as power generation and desalination, air conditioning system and moisture harvesting [8-10]. Recently, with the development of microfabrication technology, phase change heat transfer gained renewed interest [11].

Due to the high heat transfer coefficient, theories of dropwise condensation have been developed and discussed for decades. In 1936, Jakob [12] proposed that vapor condenses on the surface and forms a film of liquid at first, followed by fracture into droplets when the film reaches a certain thickness. Tammann and Boehme [13] suggested that droplet formation is a result of a nucleation and this theory was

confirmed by McCormick and Baer's experimental observation [14-16]. Umur and Griffith [17] provided an evidence which can prove that dropwise condensation is a nucleation phenomenon. They found that should there be a film existent between droplets, the thickness can't be larger than a monolayer. This work disproved the "Film Theory". Based on "Nucleation Theory", Le Fevre and Rose [18] first modeled condensation heat transfer by combining single droplet heat transfer with an overall droplet size distribution. They considered conduction resistance, vapor-liquid interfacial resistance and surface resistance in the single droplet model. McCormick and several other researchers [19-24] also modeled the dropwise condensation process. In 1973, Graham and Griffith [25] developed the expression of critical radius for dropwise condensation by using Gibbs free energy and assuming vapor at a uniform temperature. This expression was used to calculate dropwise condensation heat transfer afterward [26-28], and Wu and Maa [26] divided droplets into two regimes based on whether the droplets coalesce or not and obtained a droplet size distribution of small droplets. To improve Wu and Maa's model, Abu-Oriba [27] considered a thermal resistance of promoter coating and added it to Le Fevre and Rose's single droplet heat transfer model. Kim and Kim [29] were the first to consider hydrophobic conditions where the contact angle was greater than 90°. They found that the droplet size distribution is dependent on the contact angle. Condensation with high contact angles will cause a better performance by reducing the size of departing droplets due to a reduced friction resistance opposing gravity. Liu and Cheng [30, 31] modified Kim's dropwise nucleation model by taking into account the thermal resistance of coating, thermal resistance of liquid-vapor interface and curvature depression for nano-size droplets. They found that high contact angle will result in a high thermal resistance and large droplet nucleation radius.

The experimentally measured dropwise condensation heat transfer coefficient, however, varied widely given by researchers. Rose [32] first introduced the idea that the error is due to the presence of non-condensable gases (NCG). Many researchers have found that heat transfer performance of dropwise condensation will reduce significantly with small concentration of non-condensable gas [33-36]. Tanner *et al.* [33,34] made a comparison of dropwise condensation with non-condensable gas and demonstrated that heat transfer performance depends on the non-condensable gas components and concentration. Chung *et al*. [35] reported that with non-condensable gas, filmwise and dropwise condensation have the similar range of the heat transfer rate. Ma *et al.* [36] used a variety of non-condensable gas concentrations, sub-cooling degrees and saturation pressures to measure the heat transfer coefficient, and concluded that dropwise condensation heat transfer coefficient can decrease by 30-80% with air concentrations between 0.5-5%. Although all researchers above concluded that the effect of non-condensable gas on dropwise condensation is greater than on filmwise condensation, all of their studies were experimental. There are few theoretical studies about dropwise condensation with non-condensable gas. Huang *et al*. [37] wrote a review article for condensation with non-condensable gas, but most of the article summarized filmwise condensation. Zheng *et al.* [38] developed a single droplet model by dividing condensation processes into two parts: process of mass transfer and process of heat transfer, which are modeled by Kinetic theory, laws of continuum fluid dynamics and Fourier's law of heat conduction. Based on this model, they compared experimental results and simulation results and demonstrated the model is credible.

As over 70 % of the total heat transfer happens for droplets smaller than 10 μm [25], the occurrence of nucleation events is very important for enhancing the heat transfer

rate. There is some research involved in heterogeneous nucleation, such as Xu *et al.* [58], who studied the influence of conical microstructures for nucleation density rate (that is, temporal and spatial average of recurring nucleation events). Wen *et al.* [59] investigated the influence of non-condensable gas for the nucleation density rate. However, they mainly used numerical calculations to analyze the relationship and the supersaturation, i.e. level of sub-cooling, was low. Therefore, to investigate the performance of nucleation at higher supersaturation with the presence of non-condensable gas, we conducted experiments on dropwise condensation on a smooth hydrophobic surface at high supersaturation ratios and analyzed the relationship between nucleation density rate and supersaturation ratio. Then compared this relationship with a theoretical value based on the classical nucleation theory. We also calculated heat transfer rates at different supersaturation ratio, and analyzed the effect of non-condensable gas.

Chapter 2: Fundamentals of dropwise condensation

Dropwise condensation is one of the most complex heat transfer processes as the process is neither steady in time nor uniform in space. There are mainly four stages for single droplet condensation: 1) nucleation, 2) direct growth, 3) coalescence, and 4) departure. When a vapor contacts a sub-cooled and non-wetting (hydrophobic) surface, due to the low energy of the surface, individual droplets will form instead of a film. During dropwise condensation, vapor goes through the phase transformation at discrete nucleation sites. The size of these nucleating droplets is very small (few nm), and grow by direct condensation from the vapor above the surface. At the second stage, because the droplets are so small, the distance between any two droplets is comparatively large. So the droplets mainly grow by direct condensation from the vapor. As the droplets grow, the distance between two droplets gets smaller and droplets start to coalesce. As the droplets keep growing, their size becomes so big that the high thermal conduction resistance reduces their growth rate through direct condensation, so the growth of droplets is mainly achieved by coalescence. When the droplets reach a critical size, gravity will be larger than surface tension and surface adhesion, and droplets depart from a vertical surface in a process called sweeping. After departure, the surface will be exposed again, and the vapor will condense directly on the surface to form new nucleation sites. A new circles begins.

2.1 Classical nucleation theory

Nucleation is the first step in the dropwise condensation. There are mainly two types of nucleation: homogeneous nucleation and heterogeneous nucleation. Homogeneous nucleation occurs in the bulk of a metastable fluid (e.g., vapor), whereas heterogeneous nucleation occurs on a surface.

For the onset of the dropwise condensation process, the droplets will grow only if the radius of droplets is larger than the critical equilibrium size, which is associated with Gibbs free energy.

The Gibbs free energy, G, is a thermodynamic potential that can be used to calculate the maximum of reversible work that may be performed by a thermodynamic system at a constant temperature and pressure.

Generally, the nucleation process is described by the classical nucleation theory (CNT). In this theory, the nucleation performance is evaluated by Gibbs free energy barrier ΔG and a nucleation rate J. For homogeneous nucleation, the Gibbs free energy barrier is:

$$\Delta G_{\text{hom}} = \Delta G_v \frac{4}{3}\pi r_{\min}^{3} + \sigma_{lv} 4\pi r_{\min}^{2} = \frac{16\pi\sigma_{lv}^{3}}{3\Delta G_v^{2}}, \tag{1}$$

where ΔG_v is the change of Gibbs free energy per unit volume of the liquid, r_{min} is the critical radius of droplets, and σ_{lv} is the liquid-vapor surface tension. In a steady-state nucleation region, the homogeneous nucleation rate can be expressed by:

$$J_{\text{hom}} \sim J_0 \exp\left(\frac{-\Delta G_{\text{hom}}(r_{\min})}{k_B T_l}\right), \tag{2}$$

where J_{hom} is nucleation density rate, J_0 is a kinetic pre-factor, $\Delta G_{\text{hom}}(r_{min})$ is the Gibbs free energy barrier at critical radius r_{min}, k_B is Boltzmann constant and T_l is the system temperature.

The Gibbs free energy barrier of heterogeneous nucleation on a surface depends on the homogeneous free energy barrier and the liquid contact angle θ, so that:

$$\Delta G_{het} = \frac{2 - 3\cos\theta + \cos^{3}\theta}{4}\Delta G_{\text{hom}}, \tag{3}$$

So, the heterogeneous nucleation rate is then:

$$J_{het} \sim J_0 \exp\left(\frac{-\Delta G_{het}(r_{\min})}{k_B T_l}\right). \quad (4)$$

2.2 Changes in Gibbs free energy

For onset of droplet condensation, consider a droplet with radius r that condenses on a smooth surface at T_w with a promoter coating layer whose thickness is δ in a saturated vapor at T_s and p_s.

In order to study onset of droplet condensation further, there are two assumptions:

(i) Based on the local thermal equilibrium of the vapor and liquid before and after onset of droplet condensation, the local temperature of vapor before onset of droplet condensation is the same as after onset of droplet condensation. This means $T_v = T_l$.

(ii) When the vapor is adjacent to surface, and before onset of droplet condensation, the temperature will drop from T_s to T_v, as the pressure won't change, and the vapor will be in a supersaturated state.

The change in Gibbs free energy from supersaturated vapor to subcooled liquid is shown in Fig.1 When a supersaturated vapor at Point 2 is condensed into subcooled liquid at Point 3, the temperature is constant during this process.

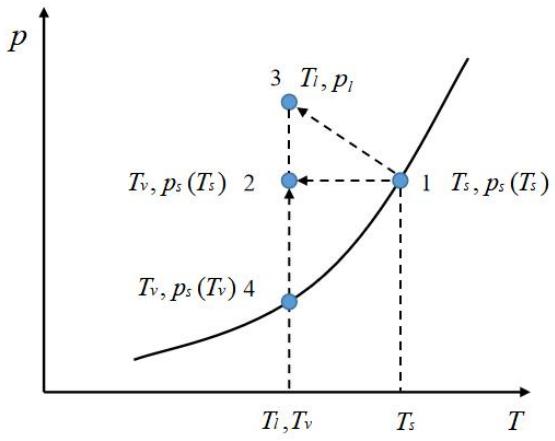

Fig. 1. Changes of Gibbs free energy during condensation process following different paths in a p–T diagram.

For a closed system, at constant temperature and pressure, Gibbs free energy is defined as:

$$G = G(T, p) = U + pV - TS, \tag{5}$$

where U is the internal energy, p is pressure, V is volume, T is the temperature and S is entropy.

Eq. (5) is the same as:

$$G = G(T, p) = H - TS, \tag{6}$$

where H is the enthalpy.

If $g = \frac{G}{m}$ is specific Gibbs free energy, it also equals:

$$g = h - Ts, \tag{7}$$

where h is specific enthalpy, s is specific entropy.

Now to determine the change of specific Gibbs free energy ($\Delta g = g_l(p_l, T_l) - g_v(p_v, T_v)$), we have:

$$\Delta g = g_l - g_v = h_l - h_v - T_l(s_l - s_v). \tag{8}$$

For the specific entropy in the second term of right-hand side of Eq. (8), we can use the thermodynamic relation:

$$ds = \frac{c_p}{T} dT - \left(\frac{\partial v}{\partial T}\right)_p dp, \tag{9}$$

where c_p is specific heat at constant pressure, and v is specific volume of the fluid. To obtain the specific Gibbs free energy of the liquid at Point 3 and the specific Gibbs free energy of the vapor at Point 2, saturated state Point 1 is introduced for simplifying the analysis. From Point 1 to Point 2, the pressure is constant ($dp=0$), the temperature will drop from T_s to T_v. The specific entropy can be given by integration of Eq. (9):

$$s_v = s_{vs} + \int_{(T_s, p_s)}^{(T_v, p_s)} ds = s_{vs} + c_{p,v} \ln\left(\frac{T_v}{T_s}\right). \tag{10}$$

The specific entropy of liquid can be given by integration of Eq. (9) from Point 1 to Point 3:

$$s_l = s_{ls} + \int_{(T_s, p_s)}^{(T_l, p_l)} ds = s_{ls} + c_{p,l} \ln\left(\frac{T_l}{T_s}\right). \tag{11}$$

According to the first assumption, $T_v=T_l$, the change of specific entropy between the vapor before nucleation and liquid after nucleation can be obtained by subtraction:

$$s_l - s_v = s_{ls} - s_{vs} + c_{p,l} \ln\left(\frac{T_l}{T_s}\right) - c_{p,v} \ln\left(\frac{T_v}{T_s}\right) = -\frac{h_{fg}}{T_s} + (c_{p,l} - c_{p,v}) \ln\left(\frac{T_l}{T_s}\right), \tag{12}$$

where h_{fg} is specific latent heat, for the change of enthalpy between the supersaturated vapor at Point 2 and the subcooled liquid at Point 3, another thermodynamic relation can be utilized:

$$dh = c_p dT + \left[v - T\left(\frac{\partial v}{\partial T}\right)_p \right] dp. \tag{13}$$

So the enthalpy of supersaturated vapor at Point 2 and the enthalpy of subcooled liquid at Point 3 are:

$$h_l = h_{ls} + c_{pl}(T_l - T_s) + v_l(p_l - p_s(T_s)), \tag{14}$$

and

$$h_v = h_{vs} + c_{pv}(T_v - T_s). \tag{15}$$

Substituting Eqs. (12), (14) and (15) to Eq. (8), and using $T_v=T_l$, we get:

$$\Delta g = g_l - g_v = \frac{h_{fg}(T_l - T_s)}{T_s} + (c_{pl} - c_{pv})(T_l - T_s) + (c_{pl} - c_{pv}) T_l \ln\left(\frac{T_s}{T_l}\right) + v_l(p_l - p_s(T_s)). \tag{16}$$

Using Taylor's series expansion to expand the third term at the right hand of Eq. (16), and keeping the first-order term, i.e., $\ln\left(\frac{T_v}{T_s}\right) = -\ln\left(\frac{T_s}{T_v}\right) \approx -(1-\frac{T_s}{T_v})$, we have:

$$\Delta g = g_l - g_v = \frac{h_{fg}(T_l - T_s)}{T_s} + v_l(p_l - p_s(T_s)), \tag{17}$$

which is also given by Quan *et al*. [39].

Eq. (17) can also be obtained by moving from saturated state at Point 4 to Point 2 for vapor, then to Point 3 for liquid. This process is isothermal (*dT=0*). The change in chemical potential can be calculated from Gibbs-Duhem equation:

$$d\mu = -sdT + vdp. \tag{18}$$

As the process from Point 4 to Point 2 is isothermal, Eq. (18) can be integrated with the ideal gas law $v_v = \frac{R_g T_v}{p_v}$:

$$\mu_v = \mu_{sv} + R_g T_v \ln\left(\frac{p_s(T_s)}{p_s(T_v)}\right), \tag{19}$$

where R_g is the specific gas constant.

From Point 4 to subcooled liquid at Point 3, since the liquid is virtually incompressible, v_l is constant. The chemical potential is:

$$\mu_l = \mu_{sl} + v_l(p_l - p_s(T_l)). \tag{20}$$

Eq. (19) and (20) were obtained previously by Khandekar and Muralidhar [40]. For a pure substance, the chemical potential per unit mass is equal to the specific Gibbs free energy. Under the assumption $T_v=T_l$, the change of specific Gibbs free energy is:

$$\Delta g = g_l - g_v = \mu_l - \mu_v = -R_g T_v \ln\left(\frac{p_s(T_s)}{p_s(T_l)}\right) + v_l(p_l - p_s(T_l)). \tag{21}$$

According to the integration of the Clausius-Clapeyron equation, the saturated pressure is：

$$\ln\left(\frac{p_s(T_s)}{p_s(T_l)}\right)=\frac{h_{fg}}{R_g}\left(\frac{1}{T_l}-\frac{1}{T_s}\right). \tag{22}$$

Substituting Eq. (22) into Eq. (21), obtain:

$$\Delta g=\frac{h_{fg}(T_l-T_s)}{T_s}+v_l(p_l-p_s(T_s))+v_l(p_s(T_s)-p_s(T_l)). \tag{23}$$

In most case, $p_s(T_s)$-$p_s(T_l)$ is very small compared with Young-Laplace equation $p_l-p_s(T_s)=\frac{2\sigma}{r}$, therefore, the third term on the right-hand side of Eq. (23) can be neglected. Based on this assumption, Eq. (23) is identical to Eq. (17).

For metastable thermodynamic equilibrium state, analysis of Gibbs free energy is a necessary process. The transition from metastable state to stable state would need to leap over an energy barrier which called critical availability change $\Delta\Psi$. Thus, the change in availability represents the work required for the transition from the metastable state to stable state. Therefore, a larger change in availability implies that the transition is more difficult to achieve [41].

The change of availability during droplet condensation is given by:

$$\Delta\Psi=\Delta G. \tag{24}$$

According to the specific Gibbs free energy, $g=\frac{G}{m}$, and thermodynamic theory of surface tension at constant temperature and pressure, $\sigma=\left(\frac{\partial G}{\partial A}\right)_{T,p}$, Eq. (24) can be modified:

$$\Delta\Psi=\Psi_l+\Psi_i+\Psi_v-\Psi_0, \tag{25}$$

where Ψ_l is the availability of the liquid, Ψ_i is the availability of the interface, Ψ_v is the availability of vapor and Ψ_0 is the initial availability:

$$\Psi_0=m_{total}g_v+(A_{sv})_i\sigma_{sv}, \tag{26}$$

$$\Psi_l = m_l\left[g_l + (p_v - p_l)v_l\right], \tag{27}$$

$$\Psi_i = A_{lv}\sigma_{lv} + (A_{sv})_f\,\sigma_{sv} + A_{sl}\sigma_{sl}, \tag{28}$$

$$\Psi_v = (m_{total} - m_l)g_v, \tag{29}$$

where g_v, g_l is the specific Gibbs free energy of the vapor phase and liquid phase, respectively, m_{total} is the total mass of the system, $(A_{sv})_i$ is the initial surface area shared by the solid and vapor of the system, $(A_{sv})_f$ is the difference between the initial surface area shared by the solid-vapor interface and the surface area shared by the solid-liquid interface.

$$(A_{sv})_f = (A_{sv})_i - A_{sl}, \tag{30}$$

so Eq. (25) is:

$$\Delta\Psi = m_l(g_l - g_v) + m_l v_l(p_v - p_l) + A_{lv}\sigma_{lv} + [(A_{sv})_f - (A_{sv})_i]\sigma_{sv} + A_{sl}\sigma_{sl}, \tag{31}$$

substituting Eq. (30) into Eq. (31):

$$\Delta\Psi = m_l(g_l - g_v) + m_l v_l(p_v - p_l) + A_{lv}\sigma_{lv} + A_{sl}(\sigma_{sl} - \sigma_{sv}). \tag{32}$$

Combine Young's equation $\cos\theta = \dfrac{\sigma_{sv} - \sigma_{sl}}{\sigma_{lv}}$ with Eq. (32), to obtain:

$$\Delta\Psi = m_l(g_l - g_v) + m_l v_l(p_v - p_l) + (A_{lv} - A_{sl}\cos\theta)\sigma_{lv}. \tag{33}$$

The areas are:

$$A_{lv} = 2\pi r^2(1 - \cos\theta), \tag{34}$$

$$A_{sl} = \pi r^2(1 - \cos^2\theta), \tag{35}$$

where r is radius of droplet and θ is contact angle of droplet.

Substituting Eqs. (34) and (35) into Eq. (33):

$$\Delta\Psi = m_l(g_l - g_v) + m_l v_l(p_v - p_l) + (2 - 3\cos\theta + \cos^3\theta)\pi r^2\sigma_{lv}. \tag{36}$$

So, combining Eq. (17) with Eq. (36) and integrating them, we get the change of availability for different droplet radii as a function of the droplet contact angle:

$$\Delta\Psi(r) = \rho_l \int \frac{h_{fg}(T_l - T_s)}{T_s} dv + \sigma_{lv}(2 - 3\cos\theta + \cos^3\theta)\pi r^2. \tag{37}$$

2.3 Determination of temperature inside the droplet

According to Fig. 2, the liquid temperature in the droplet is:

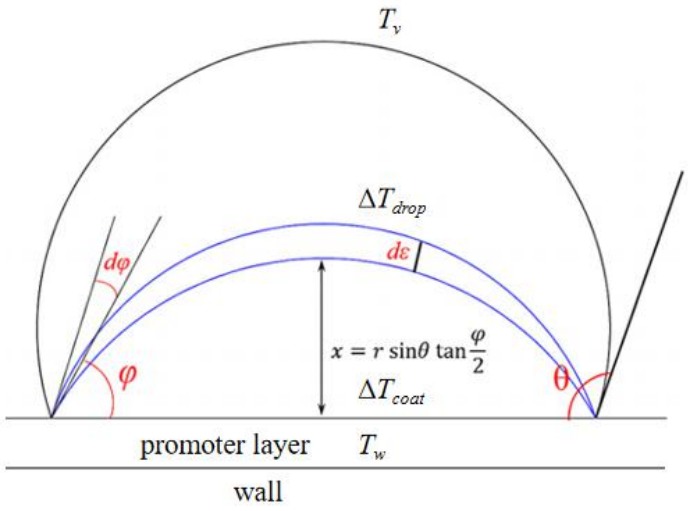

Fig. 2. Heat conduction model inside the droplet [30].

$$T_l(r;\varphi) = T_w + \Delta T_{coat} + \Delta T_{cd}(r;\varphi). \tag{38}$$

The right-hand side of Eq. (38) can be obtained from Kim and Kim [29] as follows:

$$\Delta T_{cd}(r;\varphi) = \frac{\varphi q_{cd}(r;\varphi)}{4\pi r \sin\theta \lambda_{cd}}, \tag{39}$$

$$\Delta T_{coat}(r) = \frac{\delta q_{drop}(r;\theta)}{\pi r^2 \sin^2\theta \lambda_{cd}}, \tag{40}$$

where φ is a shape-fitted coordinate for droplet, as shown in Fig.2, which depends on x and θ:

$$x = r\sin\theta\tan\frac{\varphi}{2}, \tag{41}$$

where

$$0 \le \varphi \le \theta, \tag{42}$$

Substituting Eqs. (39) and (40) into Eq. (38), we get:

$$T_l(r;\varphi) = T_w + \frac{\delta q_{drop}(r;\theta)}{\pi r^2 \sin^2\theta\lambda_{coat}} + \frac{\varphi q_{drop}(r;\varphi)}{4\pi r \sin\theta\lambda_{cd}}. \tag{43}$$

The heat transfer rate $q_{drop}(r;\theta)$ is given by:

$$q_{drop}(r;\theta) = \frac{\Delta T_{sub}\pi r^2(1-r_{\min}/r)}{\frac{\delta}{\sin^2\theta\lambda_{coat}} + \frac{\theta r}{4\sin\theta\lambda_{cd}} + \frac{1}{2(1-con\theta)h_i}}, \tag{44}$$

where h_i is interfacial heat transfer coefficient, it's defined as,

$$h_i = \frac{2\alpha}{2-\alpha}\frac{1}{\sqrt{2\pi R_g T_s}}\frac{h_{fg}^2}{v_g T_s}, \tag{45}$$

where α is condensation accommodation coefficient.

λ_{coat} is the thermal conductivity of promoter coating, λ_{drop} is the thermal conductivity of the liquid and

$$\Delta T_{sub} = \Delta T_{cd} + \Delta T_{coat} + \Delta T_{cur} + \Delta T_i, \tag{46}$$

where

$$\Delta T_{cd} = \frac{\theta q_{drop}(r;\theta)}{4\pi r \sin\theta\lambda_{cd}}, \tag{47}$$

$$\Delta T_{coat} = \frac{\delta q_{drop}}{\pi r^2 \sin^2\theta\lambda_{coat}}, \tag{48}$$

$$\Delta T_{cur} = \frac{2T_{sat}\sigma_{lv}}{\rho_l h_{fg} r} = \frac{n_0}{r}\Delta T_{sub}, \tag{49}$$

$$\Delta T_i = \frac{q_{drop}(r;\theta)}{2\pi r^2(1-\cos\theta)h_i}, \tag{50}$$

In Eq. (37), dv in terms of the local coordinate φ is:

$$dv = A_s d\bar{\varepsilon} = \pi r^3 \sin^3\theta \frac{(1-\cos\varphi)^2}{\sin^4\varphi}\, d\varphi. \tag{51}$$

Substituting Eq. (51) into Eq. (37) give:

$$\Delta\Psi(r)=\rho_l\pi r^3\sin^3\theta\int_0^{\theta}\frac{h_{fg}(T_l-T_s)}{T_s}\frac{(1-\cos\varphi)^2}{\sin^4\varphi}d\varphi+\sigma_{lv}(2-3\cos\theta+\cos^3\theta)\pi r^2. \quad (52)$$

Substituting Eq. (38) into Eq. (52) get:

$$\Delta\Psi(r)=\rho_l\pi r^3\sin^3\theta\int_0^{\theta}\frac{h_{fg}}{T_s}\left(-\Delta T_{sub}+\frac{\delta q_{drop}(r)}{\pi r^2\sin^2\theta\lambda_{coat}}+\frac{\varphi q_{drop}(r)}{4\pi r\sin\theta\lambda_{cd}}\right)\times\frac{(1-\cos\varphi)^2}{\sin^4\varphi}d\varphi+\sigma_{lv}(2-3\cos\theta+\cos^3\theta)\pi r^2. \quad (53)$$

We now obtain the critical radius r_{min} for heterogeneous droplet nucleation from Eq. (53) is:

$$\left.\frac{\partial\Delta\Psi(r)}{\partial r}\right|_{r=r_{\min}}=0. \quad (54)$$

By using Eqs. (53) and (54), the critical radius r_{min} is obtained numerically.

2.4 Heat transfer through a single droplet

For a single droplet, the thermal resistances are shown in Fig.3. The basic assumption for this model is that the resistances are independent and additive. It consists of mainly 6 thermal resistances: diffusion resistance R_{nc}, curvature resistance R_{cur}, interfacial resistance R_i, drop conduction resistance R_{cd}, promoter (or coating) resistance R_{coat} and constriction resistance R_{ct}.

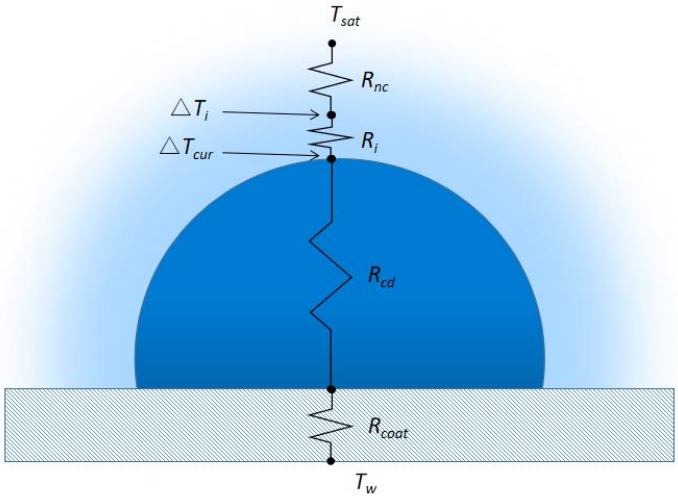

Fig. 3. Heat transfer model for single dropwise condensation

For diffusion resistance, the non-condensable gas forms a non-condensable diffusion layer which creates a temperature difference between the bulk and the liquid-vapor interface causing a diffusion barrier for vapor reaching the interface. Due to the droplets' curved surface, the saturation temperature of droplets is less than the saturation temperature of liquid on a flat surface, known as the Kelvin effect. So there is a temperature difference between a curvature surface and flat surface. At the vapor-liquid interface, there is a pressure difference (Laplace pressure) in order to drive the mass transfer across this interface. This pressure difference can be converted to a temperature difference. For a droplet larger than 10 μm, conduction resistance through the droplet plays an important role, and significantly reduces the heat transfer through the droplets. If the substrate has a promoter coating, there is a temperature drop through the promoter layer due to conduction losses as well. Since the thickness of most chemical promoters are extremely thin, this resistance can often be neglected. As for the constriction resistance, because the majority of heat is transferred through the base of small droplets, the heat flux is not uniform over the condenser surface. This resistance is significant for low conductivity condensing surfaces.

For the computation of the heat transfer through a single droplet, the temperature drop due to constriction resistance can be neglected. Thus, based on these assumption, the total temperature drop can be obtained by adding all effects of thermal resistance in series:

$$\Delta T_{sub} = \Delta T_i + \Delta T_{cur} + \Delta T_{cd} + \Delta T_{coat}, \tag{55}$$

where

$$\Delta T_{cd} = \frac{\theta q_{drop}}{4\pi r \sin\theta \lambda_{cd}}, \tag{56}$$

$$\Delta T_{cur} = \frac{2T_{sat}\sigma_{lv}}{\rho_l h_{fg} r}, \tag{57}$$

Since the wall subcooling determines the minimum viable droplet radius,

$$r_{\min} = \frac{2T_{sat}\sigma_{lv}}{\rho_l h_{fg}\Delta T_{sub}}, \tag{58}$$

Eq. (57) is reduced to:

$$\Delta T_{cur} = \frac{r_{\min}}{r}\Delta T, \tag{59}$$

$$\Delta T_{coat} = \frac{\delta q_{drop}}{\pi r^2 \sin^2\theta \lambda_{coat}}, \tag{60}$$

$$\Delta T_i = \frac{q_{drop}}{2\pi r^2(1-\cos\theta)h_i}, \tag{61}$$

Sum these equations up:

$$\Delta T_{sub} = \Delta T_i + \Delta T_{cur} + \Delta T_{cd} + \Delta T_{coat} = q_{drop}\frac{1}{\pi r^2}\frac{1}{1-r_{\min}/r}\left(\frac{\delta}{\lambda_{coat}\sin^2\theta} + \frac{r\theta}{4\lambda_{cd}\sin\theta} + \frac{1}{2h_i(1-\cos\theta)}\right), \tag{62}$$

Thus, the heat transfer rate through a drop of radius r is:

$$q_{drop} = \frac{\Delta T\pi r^2(1-r_{\min}/r)}{\frac{\delta}{\lambda_{coat}\sin^2\theta} + \frac{r\theta}{4\lambda_{cd}\sin\theta} + \frac{1}{2h_i(1-\cos\theta)}}, \tag{63}$$

Eq. (63) shows that the heat transfer rate varies with the droplet size, the contact angle, and the thickness of the coating layer.

2.5 Droplet size distribution

For an arbitrary size range r_1-r_2, the droplet growth rate is defined as:

$$Gr = \frac{dr}{dt}, \tag{64}$$

The population density of droplets $n(r)$ is defined as the number of droplets of radius r per unit area.

Assume the number of droplets that enter an arbitrary section of the condensing surface, A, is An_1Gr_1dt. The number of droplets that leave by growth is An_2Gr_2dt. The

number of droplets that leave by sweeping (or by being swept by other droplets) is $Swn_{1-2}\Delta rdt$, where Sw is the sweeping rate, $n_{1\text{-}2}$ is the average population density in the size range r_1 and r_2. Δr *is* r_1-r_2. Therefore, the number of droplets entering must equal the sum of the number of droplets leaving by growth and the number of drops swept off:

$$An_1Gn_1dt = An_2Gr_2dt + Swn_{1-2}\Delta rdt, \tag{65}$$

which can be simplified as:

$$A(n_2Gr_2 - n_1Gn_1) = -Swn_{1-2}\Delta r, \tag{66}$$

when Δr approaches to zero, $n_{1\text{-}2}$ becomes a point value, Eq. (66) can be written as:

$$\frac{d}{dr}(Grn) + \frac{n}{\tau} = 0, \tag{67}$$

where the sweeping period $\tau = \frac{A}{S}$.

The heat transfer rate through a droplet of radius r is the change of enthalpy of newly condensing vapor:

$$q_{drop} = \rho_l h_{fg} 2\pi r^2 (1-\cos\theta) Gr. \tag{68}$$

Substituting Eq. (68) into Eq. (63) can get the drop growth rate as a function of r*:*

$$Gr = \frac{\Delta T}{2\rho_l h_{fg}} \frac{1 - r_{\min}/r}{\frac{r\theta(1-\cos\theta)}{4\lambda_{cd}\sin\theta} + \frac{\delta(1-\cos\theta)}{\lambda_{coat}\sin^2\theta} + \frac{1}{2h_i}} = A_1 \frac{1 - r_{\min}/r}{A_2 r + A_3}, \tag{69}$$

where

$$A_1 = \frac{\Delta T}{2\rho_l h_{fg}}, \tag{70}$$

$$A_2 = \frac{\theta(1-\cos\theta)}{4\lambda_{cd}\sin\theta}, \tag{71}$$

$$A_3 = \frac{1}{2h_i} + \frac{\delta(1-\cos\theta)}{\lambda_{coat}\sin^2\theta}. \tag{72}$$

Integrate Eq. (67) with respect to r*,*

$$\int_{(Grn)_{\min}}^{Grn} \frac{d(Grn)}{Grn} = \int_{r_{\min}}^{r} \frac{-dr}{Gr\tau}. \tag{73}$$

By solving above equation, obtain the drop size distribution for small droplets [29]:

$$n(r) = \frac{(Grn)_{\min}}{Gr} \exp\left(\frac{A_2}{\tau A_1} \left[\frac{(r - r_{\min}^2)}{2} + 2r_{\min}(r - r_{\min}) + r_{\min}^2 \ln(r - r_{\min}) \right] + \frac{A_3}{\tau A_1} \left[r - r_{\min} + r_{\min} \ln(r - r_{\min}) \right] \right). \tag{74}$$

For large droplets, the drop size distribution $N(r)$ was established by Le Fevre and Rose [42]:

$$N(r) = \frac{1}{3\pi r^2 r_{\max}} \left(\frac{r}{r_{\max}} \right)^{-\frac{2}{3}}. \tag{75}$$

The maximum droplet radius can be estimated by the force balance between surface tension and gravity. When the drop surface is close to a circle, the capillary force can be simplified as:

$$F_c \approx cd\sigma(\cos\theta_r - \cos\theta_a) = c2r\sin\theta\sigma(\cos\theta_r - \cos\theta_a). \tag{76}$$

where θ_r and θ_a are the receding contact angle the advancing contact angle respectively. c is a numerical constant that depends on the shape of the drop and on the inclination of the substrate surface.

The gravity on the drop is:

$$F_g = \frac{2 - 3\cos\theta + \cos^3\theta}{3} \pi r^3 \rho g, \tag{77}$$

where g is gravitational acceleration.

From the balance between Eqs. (76) and (77), the radius of departure drops is:

$$r_{\max} = \left(\frac{6(\cos\theta_r - \cos\theta_a)\sin\theta\sigma}{\pi(2 - 3\cos\theta + \cos^3\theta)\rho g} \right)^{\frac{1}{2}}. \tag{78}$$

The effective radius r_e is defined as the boundary between the small droplets and large droplets:

$$r_e = (4N_s)^{-0.5}, \tag{79}$$

where N_s is droplet nucleation density, Rose [43] derived a theoretical expression for droplet nucleation density:

$$N_s = \frac{0.037}{r_{\min}^2}. \tag{80}$$

This expression, however, is seldom used in practice due to its overestimations of the number of droplet nucleation sites. Experimental values are in the range from $10^9\,\mathrm{m}^{-2}$ to $10^{15}\,\mathrm{m}^{-2}$. Note that these values refer to the initial nucleation density, not to the nucleation density rate for re-nucleating droplets that we are determining in this work. According to the continuous boundary between $n(r)$ and $N(r)$, the boundary condition is set as $n(r) = N(r)$ at $r = r_e$. This can be used to solve the unknown parameter, $(Grn)_{\min}$, and $n(r)$ is:

$$n(r) = \frac{1}{3\pi r_e^3 r_{\max}} \left(\frac{r_e}{r_{\max}}\right)^{-\frac{2}{3}} \frac{r(r_e - r_{\min})}{r - r_{\min}} \frac{A_2 r + A_3}{A_2 r_e + A_3} \exp(B_1 + B_2), \tag{81}$$

where

$$B_1 = \frac{A_2}{\tau A_1}\left[\frac{r_e^2 - r^2}{2} + r_{\min}(r_e - r) - r_{\min}^2 \ln\left(\frac{r - r_{\min}}{r_e - r_{\min}}\right)\right], \tag{82}$$

$$B_2 = \frac{A_3}{\tau A_1}\left[r_e - r - r_{\min} \ln\left(\frac{r - r_{\min}}{r_e - r_{\min}}\right)\right]. \tag{83}$$

The sweeping period τ, can be expressed as a function of r_e by adding the second boundary condition:

$$\frac{d(\ln n(r))}{d(\ln r)} = \frac{d(\ln N(r))}{d(\ln r)} = -\frac{8}{3}. \tag{84}$$

So the sweeping period become:

$$\tau = \frac{3r_e^2(A_2 r_e + A_3)}{A_1(11A_2 r_e^2 - 14A_2 r_e r_{\min} + 8A_3 r_e - 11A_3 r_{\min})}. \quad (85)$$

Despite the dropwise condensation heat transfer being a transient process, dropwise condensation heat transfer can be modeled by using a steady-state formulation which multiplies the heat transfer rate through a single droplet with the population density, then integrates the heat transfer rate through droplets at different sizes, and sums them up, leading to:

$$q'' = \int_{r_{\min}}^{r_e} q_{drop}(r)n(r)dr + \int_{r_e}^{r_{\max}} q_{drop}(r)N(r)dr. \quad (86)$$

From all above we know the temperature of the surface, which is associated with the supersaturation ratio and the per-droplet heat transfer rate, is very important in both nucleation theory and dropwise heat transfer theory. However, the calculation of this temperature is not very accurate due to the complex relationship between different thermal resistances, for example, a gap of air between substrate and coating layer would increase the thermal resistance significantly, but it is hard to quantify the thermal resistance of the gap. This uncertainty would enlarge the deviation from experiments.

So in this work, instead of calculating it, we measured the surface temperature directly by using a surface resistance temperature detector (RTD). Then combined this temperature and theories introduced before to calculate the nucleation density rate and dropwise heat transfer at supersaturation ratio. The next section will mainly introduce the design and setup of the experiment of dropwise condensation as a function of supersaturation ratio.

Chapter 3: Materials and methods

3.1 Preparation of hydrophobic surface

The nucleation density rate is related to the available surface area, such as roughness or intentionally fabricated microstructures [58] and nucleation is found to be very sensitive to chemical impurities [44], so a very small impurity can change the rate of nucleation. Mu *et al*. [45] showed that the nucleation site density of dropwise condensation increases dramatically as surface topography increase. In other words, roughness of surface will influence nucleation characteristic. Topography can also create defects on which filmwise condensation take place [46]. What's more, to sweep the surface easily and expose new area for new generations of nucleation, low contact angle hysteresis and high droplet mobility are necessary [47]. But the roughness influences both the static contact angle and contact angle hysteresis (difference between the advancing and receding contact angle). With the increase in the roughness, the advancing contact angle will increase and the receding contact angle will decrease [48]. In order to eliminate these influences, we conducted dropwise condensation on a smooth and hydrophobic solid surface. A polished Silicon wafer is an ideal material as a substrate due to it's small roughness (around 2 nm). In this experiment, 4 inch diameter polished silicon wafer (<100> orientation, TED PELLA, Inc) with 500 μm thickness is utilized as substrate. However, silicon is hydrophilic, so a promoter must be used to create a hydrophobic surface. To promote dropwise condensation, a low-energy coatings such as polytetrafluoroethylene (Teflon, PTFE) or hexadecyltrimethoxysilane (HTMS) can be used as promoter. Thus, the silicon wafer was cut into 15 mm by 15 mm size. Then rinsed wafer with acetone, IPA, and deionized (DI) water and blown dry with nitrogen gas. Afterwards, the silicon wafer

was placed in an O2 plasma (Plasma-Preen II-862, Plasmatic Systems, Inc) for 30 seconds to remove organic contamination left on substrate and to create OH groups at the surface. Subsequently, the activated silicon chip was put in a container alongside an HTMS solution (volume ratio of HTMS to Toluene is 1/9) and another larger container was covered on top to seal the container. Finally, the container was placed in the oven at 100 ℃ at atmospheric pressure for 4 h. The HTMS evaporated from solution and deposited on the silicon chip surface. After deposition, pictures of water contact angles were captured by using a Nanomite Programmable Syringe Pump (Harvard Apparatus, Inc) and a Canon EOS Rebel T6i camera. ImageJ was used to measure the contact angle. The setup is shown in Fig. 4.

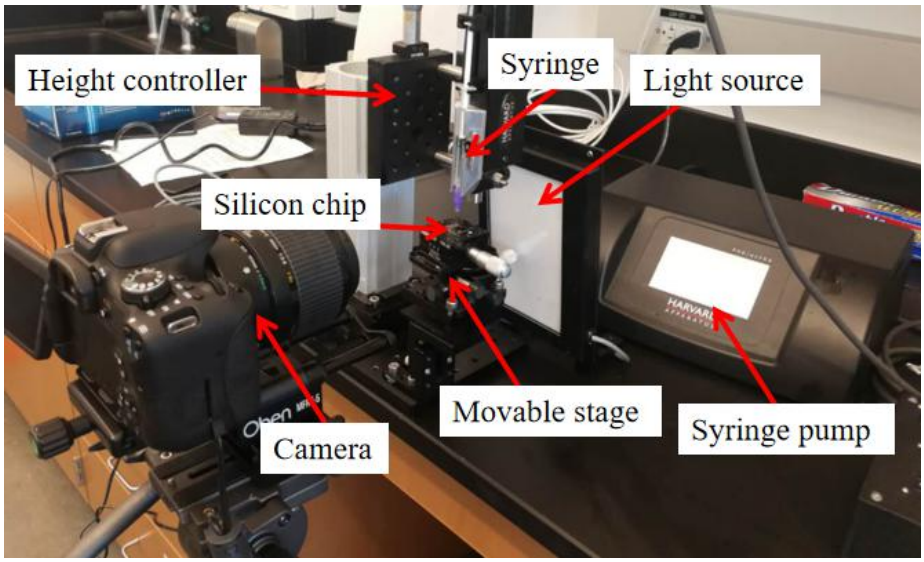

Fig. 4. Setup of contact angle measurement

The static, advancing and receding contact angle are 105 degrees, 111 degrees and 97 degrees respectively (the deviation is 2 degrees), as shown in Fig. 5. The hysteresis is around 14 degrees which is relative low, so the droplets' mobility is high.

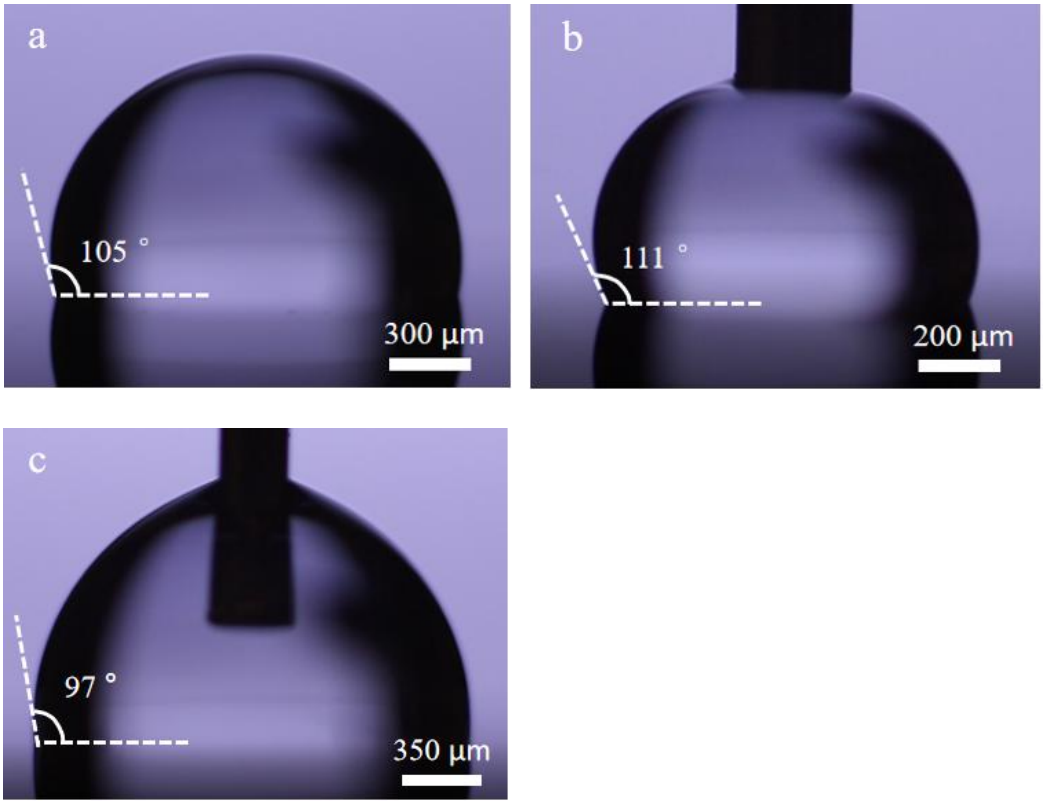

Fig. 5. Contact angles on surface of HTMS. (a) Static contact angle. (b) Advancing contact angle. (c) Receding contact angle.

3.2 Experimental setup

To enhance droplet sweeping and promote frequent re-nucleation, we conducted dropwise condensation experiments on vertical surface. Therefore, a chamber was designed for experiment, as shown in Fig. 6. In order to create a subcooled vertical surface which has constant temperature, a copper block was applied to reduce the thermal resistance between the sample and the coolant. The Silicon chip was mounted on the copper block with silver paste. To prevent heat transfer between the chamber and the ambient environment, top insulation, bottom insulation and block cover were introduced. The insulation was made of acrylic. Furthermore, the top insulation between the cold plate and the top cover is hollow inside, as the air inside the cavity adds an extra thermal resistance which can prevent heat transfer. The block cover 3D printed with plastic, and also has a hollow structure to minimize lateral heat losses

from the copper block to the vapor in the chamber. To image the dropwise condensation, a metal top cover with a window was used. A vapor-gas mixture was supplied through side fittings. As mentioned before, to reduce the deviation of calculation for temperature of surface, a surface RTD and a air RTD were mounted in chamber to measure the temperature of surface and vapor, respectively. To measure the relative humidity, an relative humidity probe was also installed in the chamber.

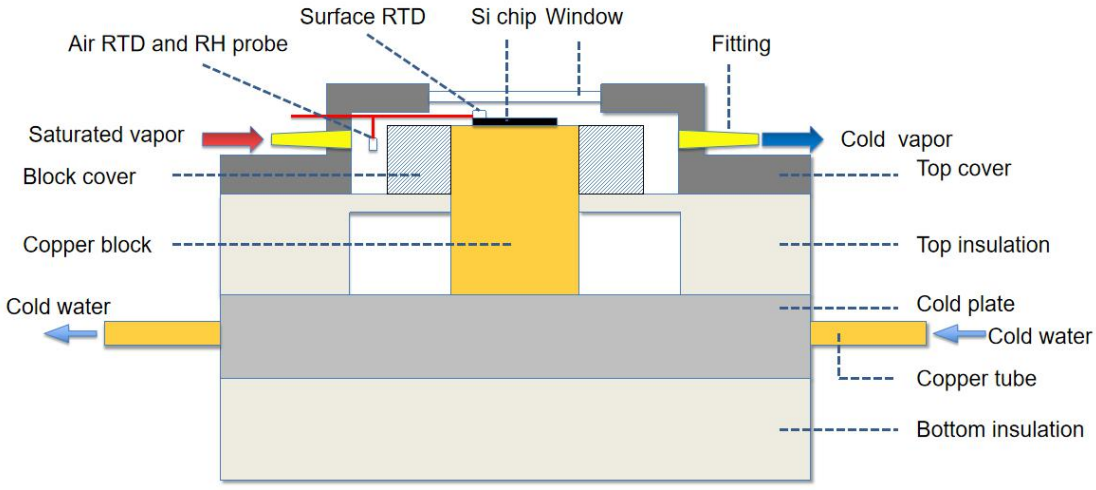

Fig. 6. Cross section of chamber.

The schematic of experiment setup is shown in Fig. 7. The cold plate was connected to an external chiller, which supplied cold circulating water to cool the copper block. A flask containing deionized water (DI water) was heated on a hot plate. Compressed nitrogen gas at 12.5 liters per minute (LPM) was supplied to the flask. It saturated with vapor and was transferred to the chamber through a plastic tube covered with fiberglass insulation. The dropwise condensation was monitored by Photron FASTCAM Mini AX200 high-speed camera which was mounted on DIY Cerna Microscope (Thorlabs). To analyze micro-scale droplets, a 100× brightfield objective was used. As the microscope only can mount lens in the vertical direction, a 90° angle mirror was applied to reflect the light path horizontally. The temperatures of surface and chamber were measured by two calibrated resistance temperature detectors (RTD),

connected to RTD reader (OctRTDTempV2, MadgeTech Inc). Since edge effects can strongly effect droplet growth [49], we mounted a surface RTD on one corner of the silicon chip and visually observed only middle region. The relative humidity (*RH*) in the chamber was measured by an *RH* probe (PCMini52, MICHELL Instruments) with an accuracy of 1%, and was held close to 100%. The temperature difference between the interior of the chamber and the ambient can easily cause condensation on the window, so an annular thin film heater was attached on the window to prevent condensation. Fig. 8-10 show pictures of the actual setup.

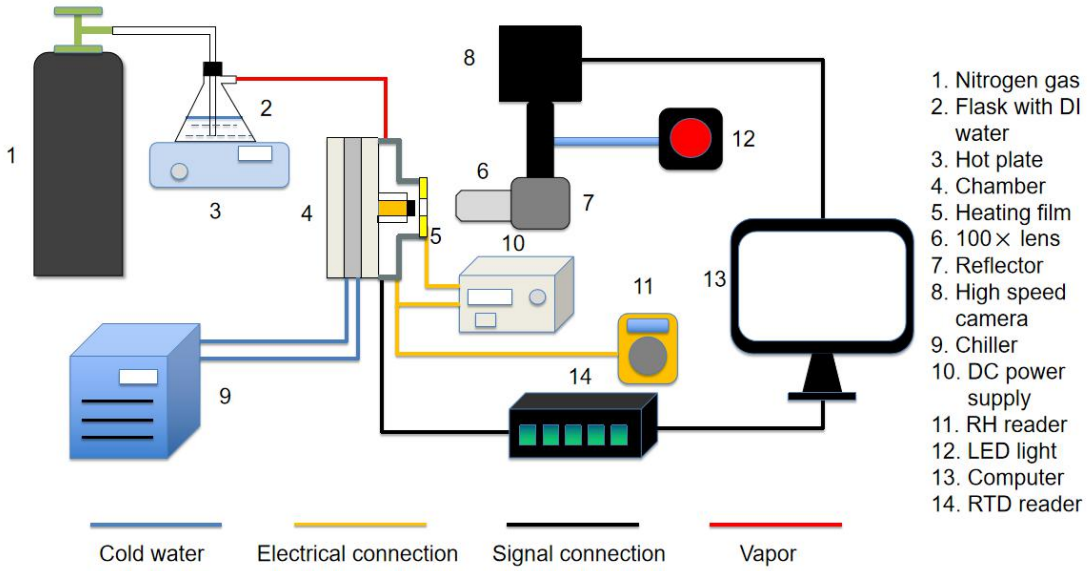

Fig. 7. Schematic of experiment setup.

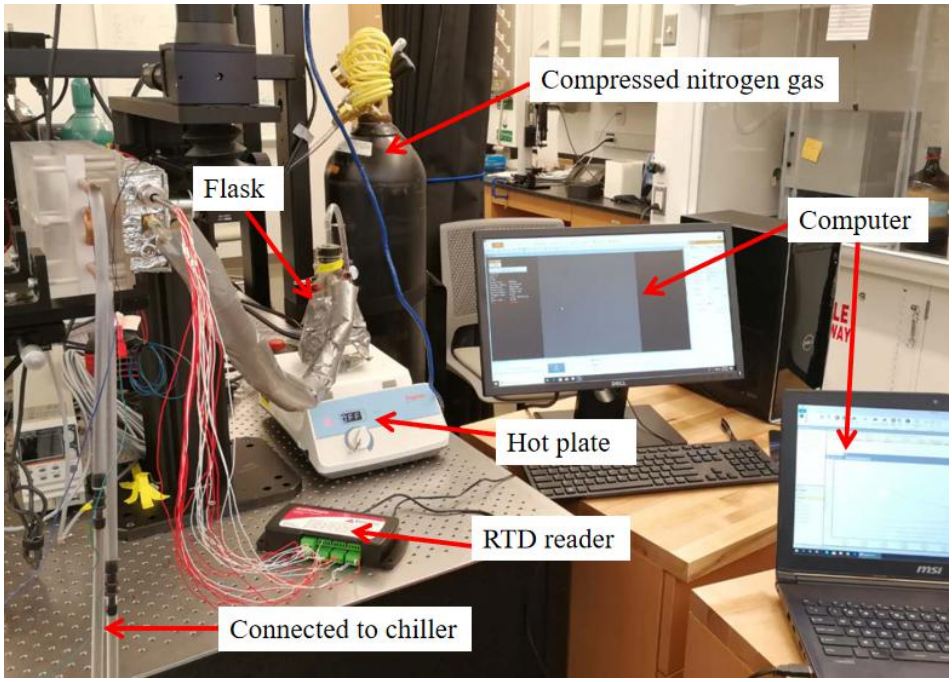

Fig. 8. Experiment setup (Part I).

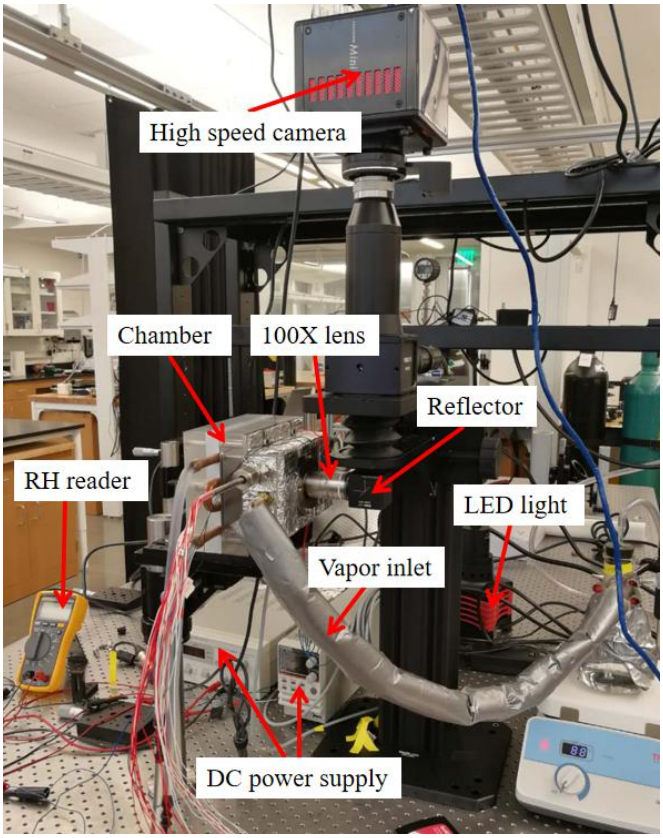

Fig. 9. Experiment setup (Part II).

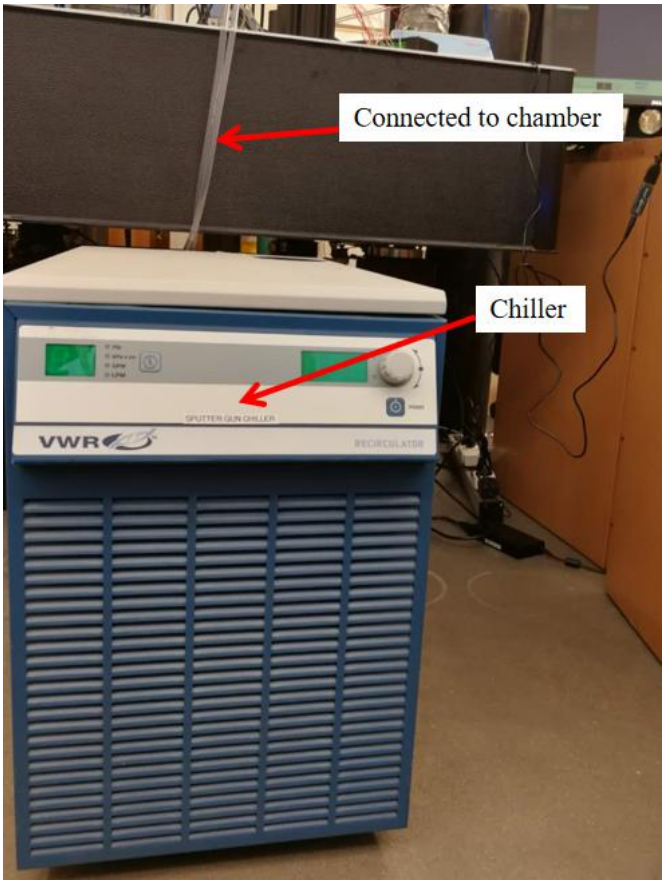

Fig. 10. Experiment setup (Part III).

3.3 Statistical analysis of nucleation density rate

To conduct dropwise condensation at different supersaturation ratios, experiments were conducted at 4 different vapor temperatures: 35℃, 45℃, 55℃ and 65℃. Each experiment was recorded with the camera at 50 fps. In order to detect the smallest possible droplets, a 100× objective lens was used. The minimum detectable diameter of droplet for 100× is approximately 1 μm, which is larger than the minimum nucleation radius, but smaller than the critical coalescence radius r_e. At each temperature, we selected at least 10 locations randomly and recorded each location with duration about 7 minutes. For each video, 4 random 400 × 400 pixels interest regions, that is 5.476×10^{9} m^2, were extracted for counting the nucleation numbers manually. Finally, the average nucleation density rate at different temperature were calculated from data.

Chapter 4: Results and discussion

4.1 Hydrophobic surface coating and test

To rule out the effect of topography, we first tried the smoothest know surface: mica (Highest quality Grade V1, TED PELLA, Inc). After several failed approaches to coat mica with a hydrophobic coating (see below), we switched to polished silicon wafers (4 inch, one side polished, TED PELLA, Inc). The roughness of these two surfaces was measured by atomic force microscopy (AFM), and the Gwyddion software was used to analyze the roughness, as shown is Fig. 11. From the Fig. 11, it is clear that the roughness of both surfaces are less than 10 nm. And the roughness average (R_a) of silicon wafer and mica are 2.78 nm and 2.95 nm, respectively. So both are adequate substrates for our experiment.

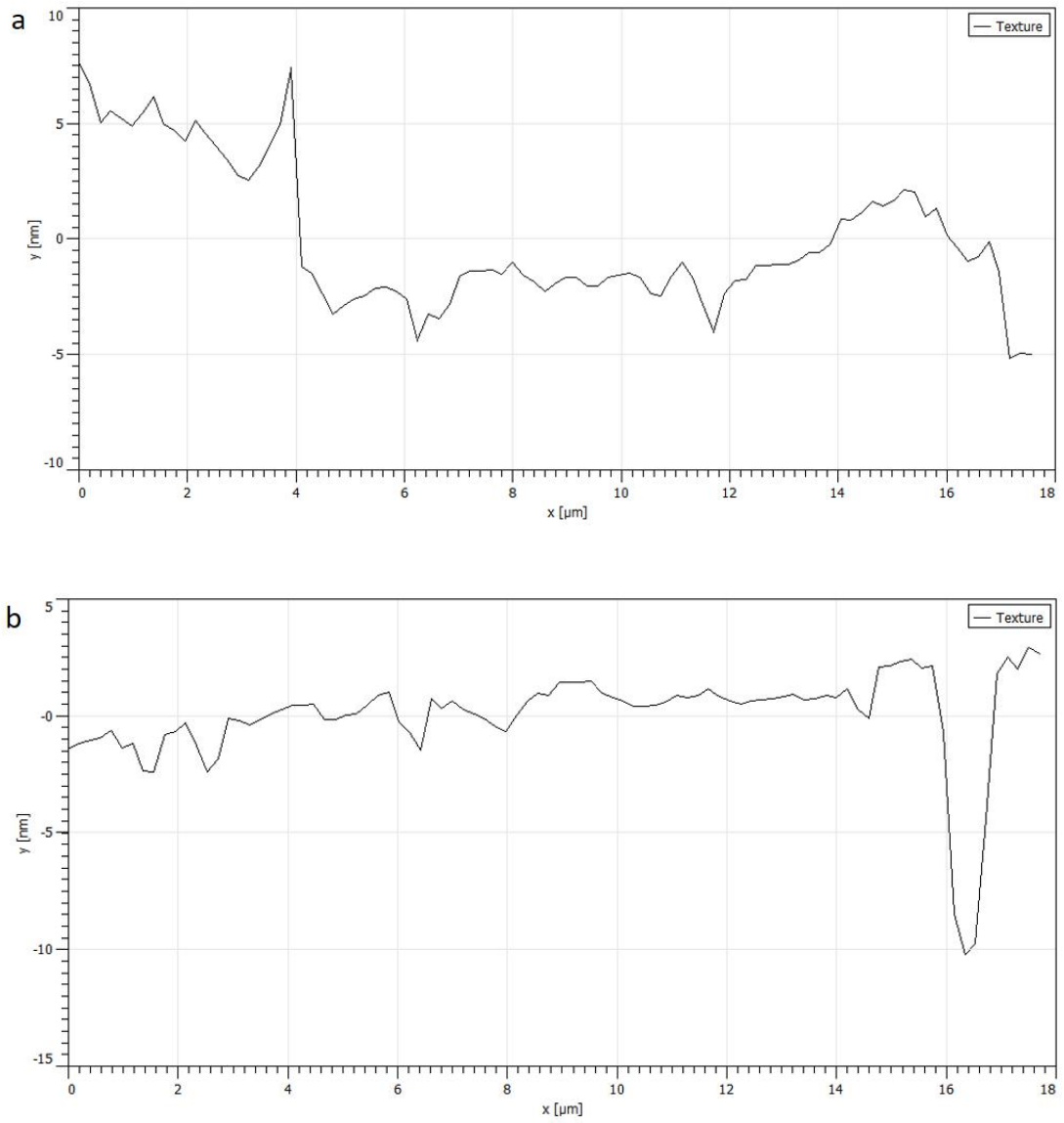

Fig. 11. Roughness measured by AFM. (a) roughness of silicon. (b) roughness of mica.

As mentioned before, as both surfaces are naturally hydrophilic, a hydrophobic surface needs to be coated on them. We used two approaches: a 10% concentration HTMS (0.3 ml HTMS and 2.7 ml toluene) and a 2% concentration Teflon (0.2 ml 6% concentration Teflon AF 1601 solution and 0.4 ml FC-40).

HTMS can bond with hydroxyl on surfaces with vapor deposition. Fig. 12 is the chemical reaction of anhydrous deposition of silanes. However, the surface of mica is devoid of reactive groups, thus organic molecule such as chloro-, ethoxy-, and

methoxysilanes are difficult to form covalent attachment on mica surface [50] even though treated by oxygen plasma. Fig. 13 shows the vapor condensation on a mica after coating HTMS. The shape of droplets is not circular, indicating that the HTMS coating is of low quality. Although the plasma produced from water vapor could potentially active the surface of mica by hydroxylation [51], we don't have those capabilities in our lab.

For Teflon solution coating, we used a spin coater with 1000 revolutions per minute (rpm), 1500 rpm, and 3000 rpm for 15s, then placed the coated mica in an oven to bake for 10 minutes at 165 ℃ to ensure its glass transition, and finally measured the roughness and promoter thickness with AFM and profilometry, respectively. Table 1 shows the Teflon thickness at different rpm. When rpm is around 3000 rpm, the thickness of Teflon is too thin to form a stable coating. Teflon coating can form dropwise condensation, and the roughness of coating is less than 20 nm (Fig. 14), but the adhesion is weak. Fig. 15 shows the weak adhesion of Teflon coating on mica, indicated by the delamination of the coating during condensation experiments. Beneath the coating, it's clear to see some apertures. These apertures is made from departure between coating and mica. To illustrate the weak adhesion, there are four regions (1, 2, 3, and 4) in Fig. 15a. After 5 seconds, region 1 and region 2 combined together and form region 5. Region 3 and 4 also coalesced and form single aperture region 6. In order to solve the problem of adhesion, instead of spinning coating, a plasma enhanced chemical vapor deposition (PECVD) could be utilized [52]. This method use fluorocarbons such as CF_4, C_2F_6 and C_4F_8 as source materials to deposit organic polymers like C-F bonds on surface of mica. But this process needs very high source power (2 kW) and very low pressure (10^{-6} Torr) which is out of scope of the instrument in our cleanroom.

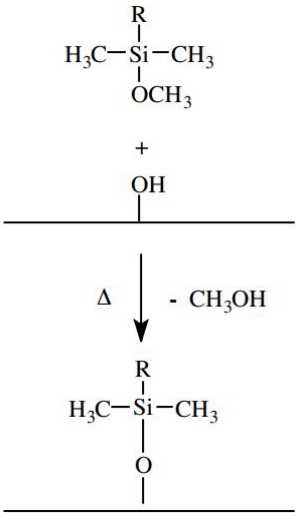

Fig. 12. Vapor deposition of silanes, silicon will bond with oxygen to form covalent bond by heating.

Table. 1. Thickness of Teflon coating at different rpm.

rpm	Thickness (μm)
1000	2
1500	1.5
3000	less than 0.5

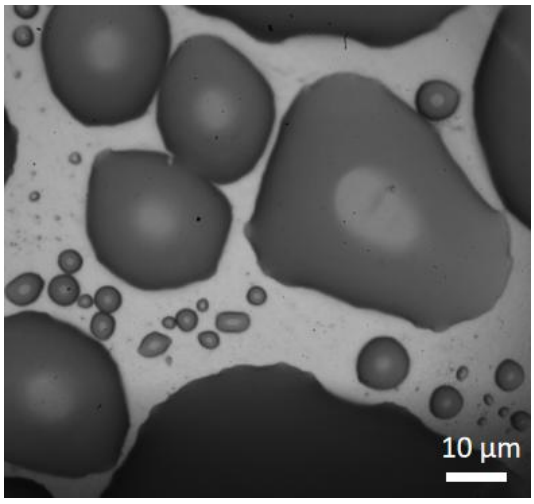

Fig. 13. Vapor condensed on mica with HTMS coating. The wettability of surface is hydrophilic due to failure of coating HTMS on mica.

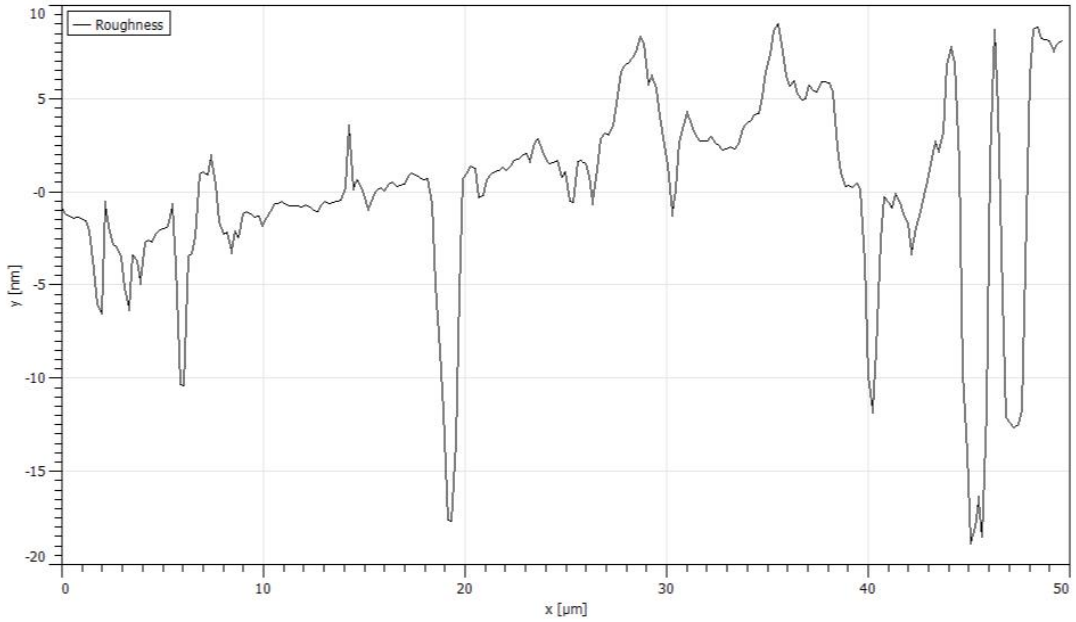

Fig. 14. Roughness of Teflon coating measured by AFM.

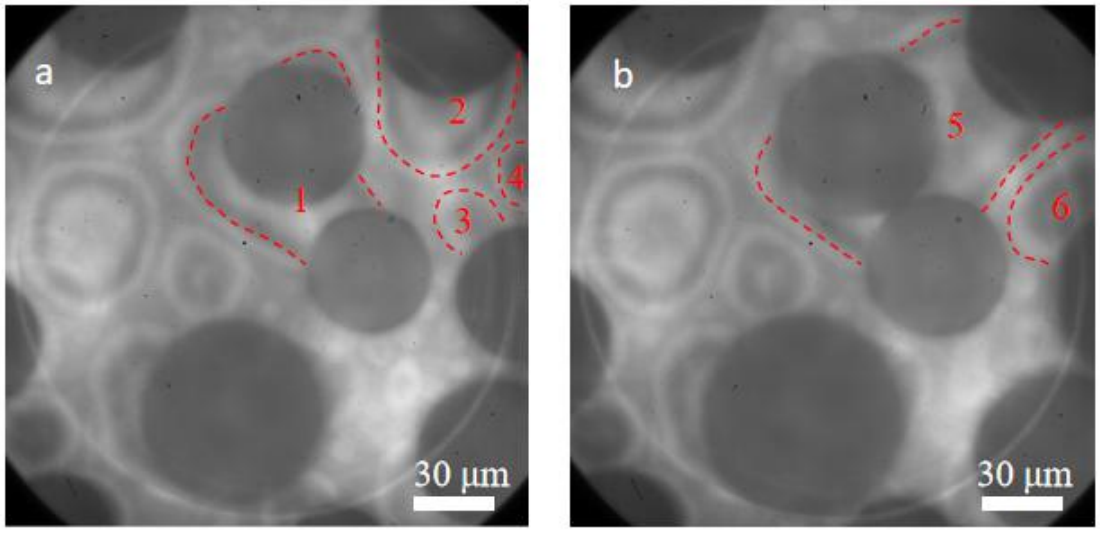

Fig. 15. Two images of dropwise condensation on mica with Teflon coating at the same location in 5 seconds interval.

There are also some other methods for hydrophobic promoter coating on mica, for example ion beam sputtering by using low energy Ar^+ to bombard the surface of mica. This process can lead to topographical and physicochemical change of the surface which are responsible for the low wettability [53]. But sometimes the static contact angle is less than 90 degrees, i.e. hydrophobicity is not reached. Stearic acid (STA)

vapor deposition can be conducted in oven at atmospheric pressure [54]. The drawback for this process is the heterogeneous coating for both monolayer film and multilayer films, which may lead to parts of the mica surface being exposed to the environment. Physical vapor deposition (PVD) of Teflon utilizes RF magnetron sputtering in Argon equipped with Teflon target [55]. This process can produce superhydrophobic surfaces, however, the roughness will increase after deposition. A hydrophobic monolayer film of Octadecyltriethoxysilane (OTE) can be coated on mica by using Langmuir—Blodgett deposition [50]. Unfortunately, the mica also need to be treated with plasma produced from water vapor.

Based on all the information above, we instead switched to using a silicon wafer as substrate and HTMS as coating material. The details of coating is described in section 2.1. What needs to be mentioned here is the vapor deposition of HTMS barely changes the topography and other characteristic of surface, so the roughness of HTMS coating didn't change much compared to the roughness of the uncoated silicon wafer.

4.2 Time evolution of nucleation density rate

To analyze the relationship between nucleation density rate and supersaturation ratio, we first examined how the nucleation density rate evolved with time at 35℃, 45℃, 55℃, and 65℃. Fig. 16 shows the nucleation density rate versus time. At 35℃ and 45℃, the sweeping cycles are so long that the maximum record duration (7 minutes) based on the internal memory of the Photron camera was applied to record the videos. For 55℃ and 65℃, the time during sweeping cycle reduced dramatically. So the duration of 2 minutes and 1 minutes were used at 55℃ and 65℃, respectively.

We randomly select 9 videos at each temperature and calculated the evolution of nucleation density rate over time. According to Fig.16, there are two types of trends for the lines: 1) the nucleation density rate are high at the beginning, then decrease

slowly and finally become stable. 2) the nucleation density rate is low in the beginning, then increases at some point significantly, and finally stabilizes at a certain value. The black circles shown in Fig. 16 are the points in which the nucleation density rate increases sharply. The reason is sweeping or coalescence processes for big droplets, as shown in Fig. 16e and Fig. 16f. When a sweeping or coalescence of big droplets happens, the subcooled surface will be exposed to supersaturated vapor, which causes the generation of new nuclei in a very short time. What's more, after a sharp rise of nucleation density rate, it starts to decrease slowly. During this period, coalescence of small droplets play a major role. When the droplets grows larger, the new droplets start to coalesce, which can offset a portion of the reduction of nucleation density rate till next sweeping or coalescence of large droplets. Although the plots shows that the nucleation density rate is transient and varied at the beginning, the overall, average nucleation rate density converges to a given value, as dropwise condensation is a cyclic process. Compared these plots to each other, it is obvious that at 35℃ and 45℃, the rise speed for type 2 lines is slower than at 55℃ and 65℃. The main reason is the difference of growth rate for droplets and nucleation density. As the temperature increases, the growth rate for small droplets increases significantly, in other words, coalescence take place more frequently and eventually leads to shortening the period of successive sweeping cycles, as shown in Fig. 17. From analyzing 40 videos and averaging the sweeping frequency at different temperature, it is clear that the frequency increases exponentially with a rise in temperature. The nucleation density is related to minimum droplets size (Eq. (58)). With the rise of temperature and the increase in sweeping frequency, the minimum droplets size will be smaller. Based on Eq. (80), the smaller the size, the greater the nucleation density. Therefore, both aspects influence the nucleation density rate at different temperatures.

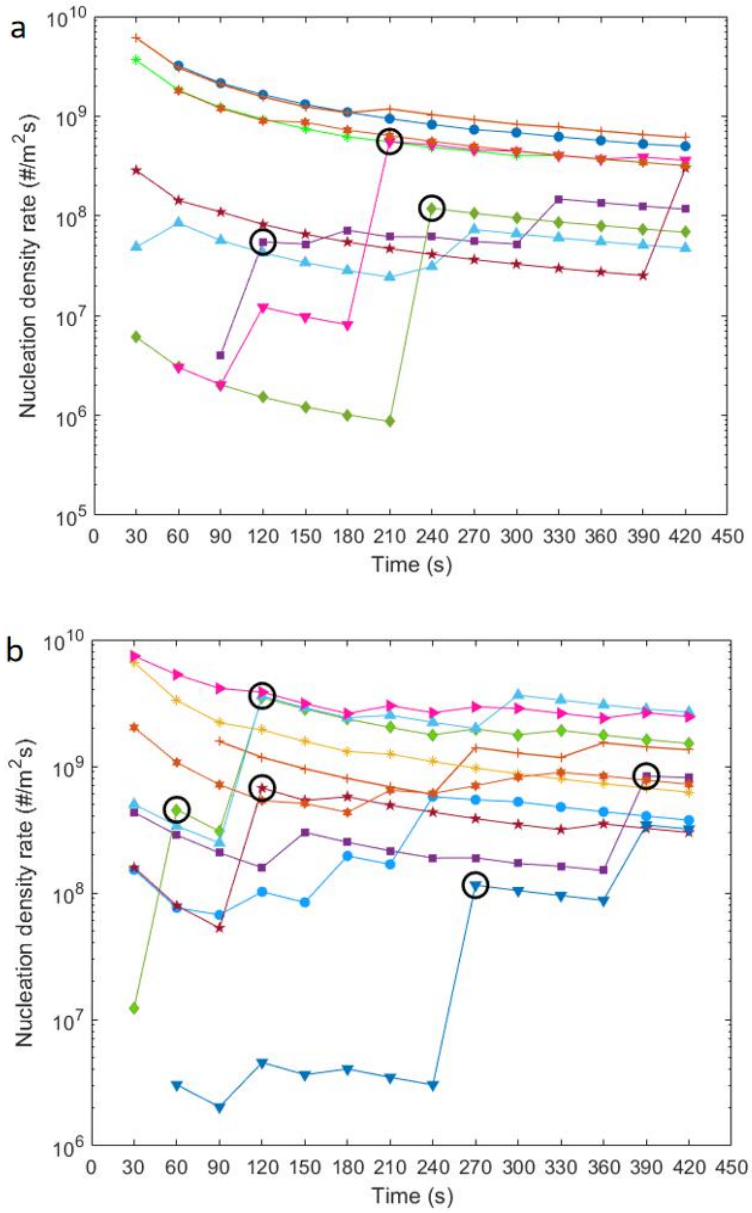

Fig. 16. Nucleation density rate evolve with time. The vapor temperature from (a) to (d) are 35℃, 45℃, 55℃ and 65℃ respectively. (e) Big droplet before coalesce. (f) Nucleus formed after big droplet coalescence.

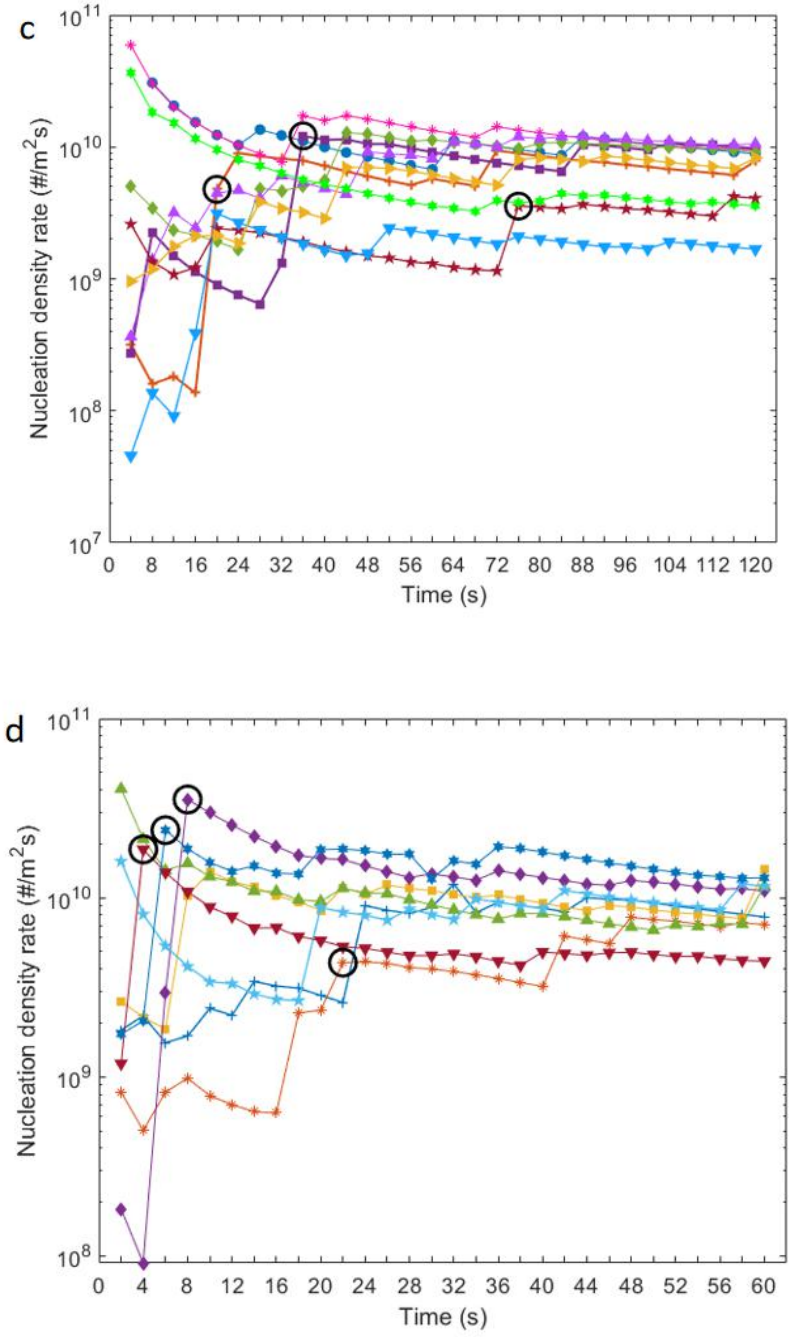

Fig. 16 (continued).

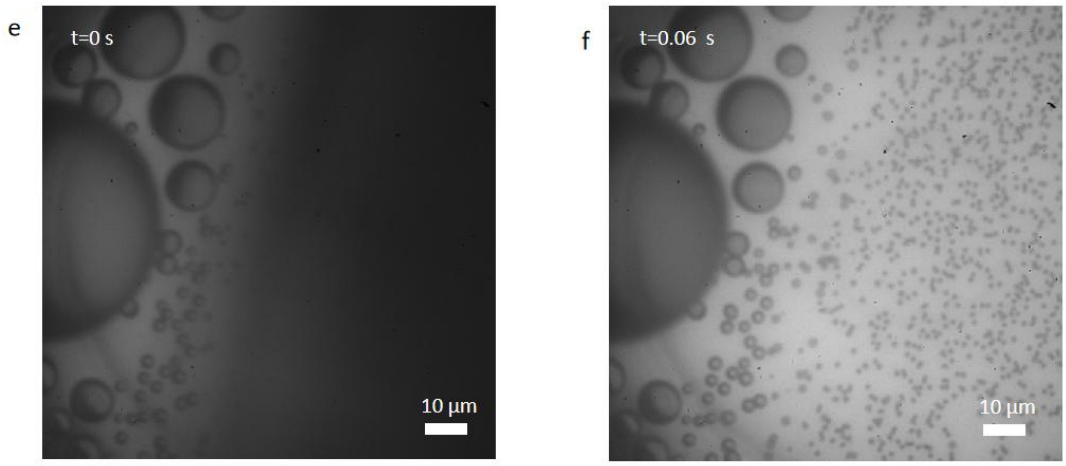

Fig .16 (continued)

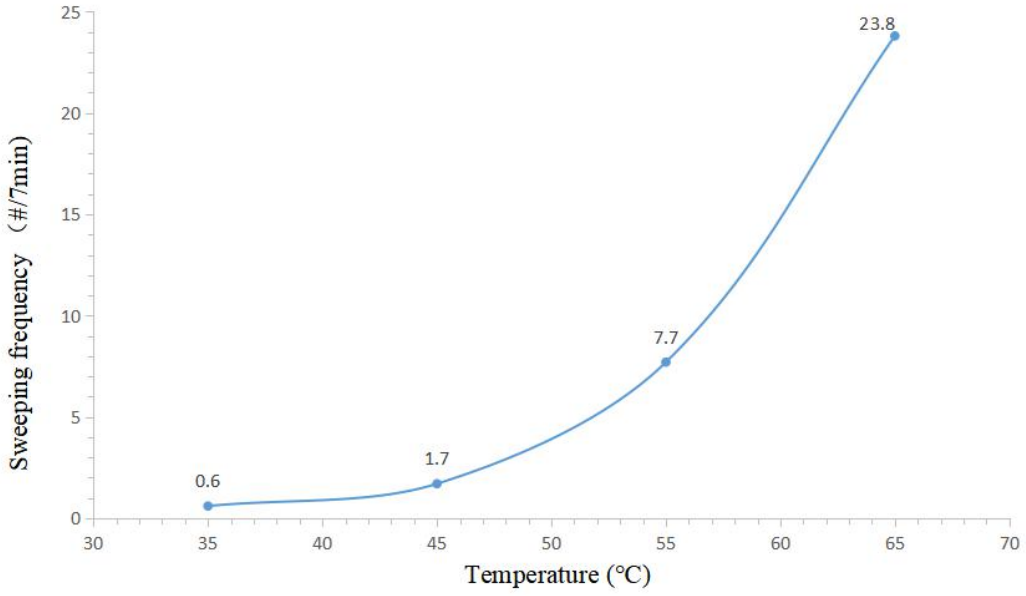

Fig. 17. Sweeping frequency increases exponentially with rise of temperature.

4.3 Nucleation density rate at different supersaturation ratio

We ran the experiments at a series of supersaturation ratios (*SR*) in the chamber. The supersaturation ratios is defined as:

$$SR = \frac{p_v}{p_{vs}}, \tag{87}$$

where p_v is the vapor partial pressure at T_v, and p_{vs} is the saturated vapor pressure at the silicon surface (T_w). By analyzing all the data we collected in different videos, the relationship between nucleation density rate and supersaturation ratio is generated, as

shown by the red dash line in Fig. 18. The horizontal error bars are from the fluctuation of vapor and substrate temperatures and the vertical error bars are the standard deviation of nucleation density rate measured from experiments. From Fig. 18 we can see that with increase of the supersaturation ratio, the nucleation density rate grows exponentially. So the nucleation density rate at the high supersaturation ratio is two orders of magnitude larger than at low supersaturation.

We also calculated theoretical values on the basis of classical nucleation theory.

In Eq. (1), ΔG_v can be given by [56]

$$\Delta G_v = -n_l k_B T_l \ln\left(\frac{p_v}{p_s}\right), \tag{88}$$

where p_v and p_s are the partial and equilibrium pressure of water vapor at temperature T_l, respectively. n_l is the number of molecules per unit volume of the liquid, and critical radius can be calculated by using Kelvin's classical equation:

$$\ln\left(\frac{p_v}{p_s}\right) = \frac{2\sigma_{lv}}{n_l k_B T_l r_{\min}}. \tag{89}$$

Combining Eq. (1), Eq. (88) and Eq. (89), we obtain the homogeneous Gibbs free energy barrier. So we can use Eq. (3) to calculate the heterogeneous Gibbs free energy barrier.

The heterogeneous nucleation density rate can be calculated by using Eq. (4). The kinetic pre-factor J_0 depends on the vapor condition and nucleus configuration [57], which is

$$J_0 = \left(\frac{p_v}{k_B T_l}\right)^{\frac{5}{3}} v\left(\frac{2\sigma_{lv} m}{\pi}\right)^{\frac{1}{2}} \frac{1+\sin(\theta-\beta/2)}{2\sqrt{F(\theta,\beta)}}, \tag{90}$$

where m is the mass of one molecule, $F(\theta,\beta)$ is a factor related to substrate structure parameters, it is given as follows:

$$F(\theta,\beta)=\frac{1}{4}\left[2+3\sin\left(\theta-\frac{\beta}{2}\right)-\sin^3\left(\theta-\frac{\beta}{2}\right)-\cos^3\left(\theta-\frac{\beta}{2}\right)\cot\frac{\beta}{2}\right], \quad (91)$$

θ *and* β are contact angle and cone angle respectively. As the surface of the sample is very smooth, $\beta \approx 180°$ on a planar substrate.

Based on the above equations, we got the heterogeneous nucleation density rate, as shown in the blue line in Fig. 18.

However, from Fig. 18 we found the theoretical values of nucleation density rate is higher than that the experimental data, especially at high supersaturation rate. Compared with experiments, the theoretical nucleation density rate at 65℃ is increased around 9.4×10^7 times. Although both of growth patterns are exponential, the growth rate of the theoretical line is faster than the experimental one. In other words, higher the supersaturation ratio is, larger the gap of nucleation density rate is.

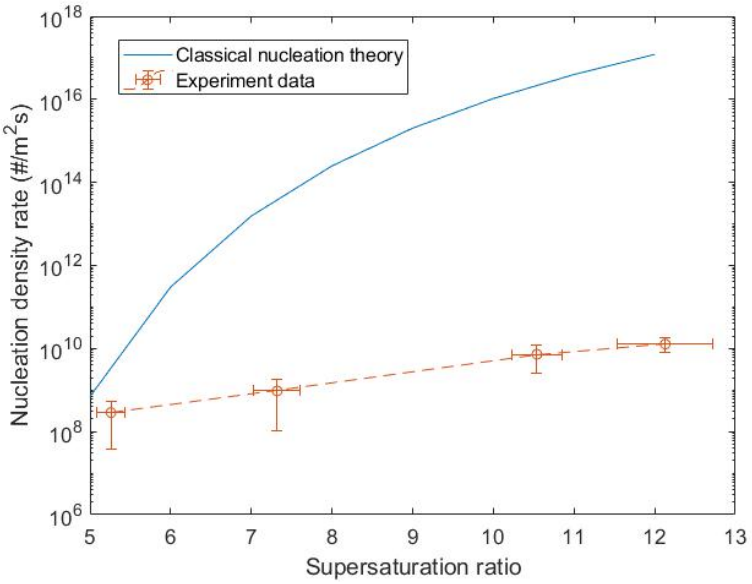

Fig. 18. Experimental and theoretical nucleation density rate at different supersaturation ratios.

The most important reason for the difference nucleation density rate is the presence of non-condensable gas. In this experiment, we used nitrogen gas to transport vapor into the chamber. The non-condensable gas can accumulate near the surface and form a

diffusion layer that reduces the density of vapor. Non-condensable gas also reduces the partial pressure p_v, which is associated with supersaturation p_v/p_s. In classical nucleation theory, the supersaturation has a strong effect on the nucleation density rate. For low supersaturation ratio, the difference between p_v and p_s is small, but for high supersaturation ratio, the decrease of partial pressure will strongly influence the nucleation energy barrier ΔG_{het}. Wen's [58] studied the influence of non-condensable at the supersaturation of 2 by using numerical calculations. They found for a 120° contact angle's surface, if the concentration of non-condensable gas increases from 0 to 30%, the nucleation energy barrier increases from 2.4×10^{-19} J to 8.6×10^{-19} J, and therefore the nucleation density rate will reduce by up to 3×10^{13} . Their calculation also demonstrated that at high supersaturation, the non-condensable gas strongly influences the nucleation density rate.

Another explanation is the underestimation of the real nucleation rate density due to experimental limitations. For 100× lens, we can only tell the nucleus whose diameter is around 1 μm. However, according to Eq. (89) or Eq. (58), the critical radius at high supersaturation ratio is on the order of nanometers, which is much smaller than the diffraction limit for visible microscopy. We are thus not able to detect droplets that coalesce prior to reaching 1 μm, potentially underestimating the nucleation density. Fig. 19 shows the nucleation process within a certain time after the coalescence of a big droplet. In Fig. 19a, even though it is only 0.014 second after the coalescence happened, the nuclei have already formed in Fig. 19b, and they keep merging into larger droplets quickly due to the very high nucleation density. The coalescence of small droplets are very frequent, as can be seen from the color change (darkening or blurring) . In Fig. 19d, even though the size of droplets is around 1 μm, it is hard for us to analyze the exact droplet density owing to the high packing of droplets.

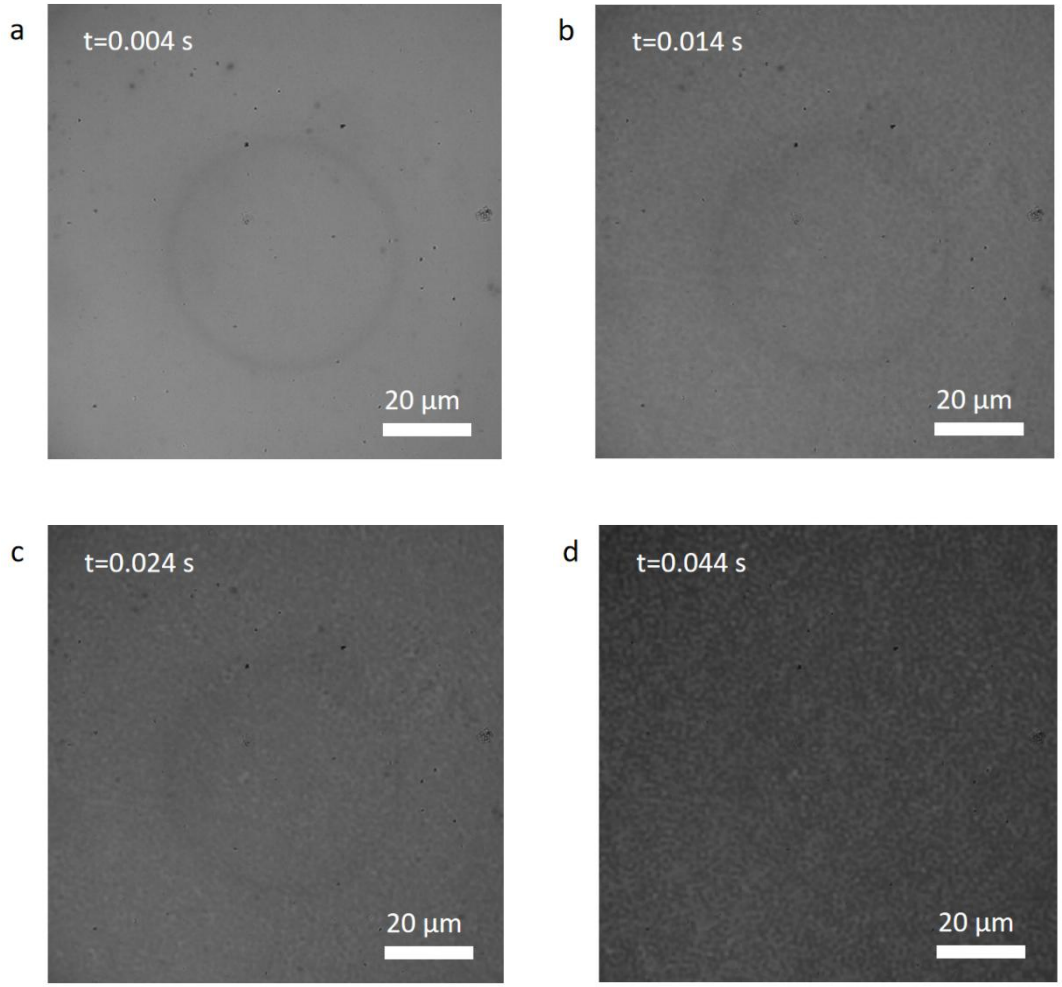

Fig. 19. Nucleation within a certain time after coalescence of big droplets.

4.4 Heat transfer performance at different supersaturation ratios

Based on the nucleation density rate we measured and Rose's model for the distribution of larger droplet sizes, the heat transfer rate is analyzed.

Here, as the thickness of the coating is very thin, the thermal resistance of coating is neglected. Eq. (63) can be modified to

$$q_{drop} = \frac{\Delta T \pi r^2 (1 - r_{\min}/r)}{\frac{r\theta}{4\lambda_{cd}\sin\theta} + \frac{1}{2h_i(1-\cos\theta)}}. \tag{91}$$

where ΔT is the subcooled temperature. Instead of calculating ΔT by using Fourier's law through the copper, we measured the temperature of substrate directly.

For the distribution of small droplets ($n(r)$ in Eq. (86)), we used the measured values for the nucleation density rate. For the size distribution of larger droplets ($N(r)$), Eq. (75) is utilized. Therefore the total heat flow rate can be calculated by using Eq. (86). The relationship between supersaturation ratio and heat flow rate is shown in Fig. 20. In Fig. 20, there are two lines, and both have the same parameters except small droplets distribution $n(r)$. For blue dash line, we used experimental values as small droplets distribution, for orange dash line, we used Eq. (81) as small droplets distribution. As the supersaturation ratio rises, the nucleation density increases, which can lead to rise of heat transfer. Although the heat flow rate is proportional to supersaturation ratio in both lines, theoretical values are larger than experimental values. The main reason for this is the difference of small droplets density between theoretical values and experimental values, and this difference is caused by non-condensable gas. In experimental values, we measured the droplets density whose size around 1 micron and used it as the density of small droplets. However, in theoretical values, the density of small droplets is larger than measurements, Therefore, in Eq. (86), the heat flow rate of small droplets is higher than that in experiment.

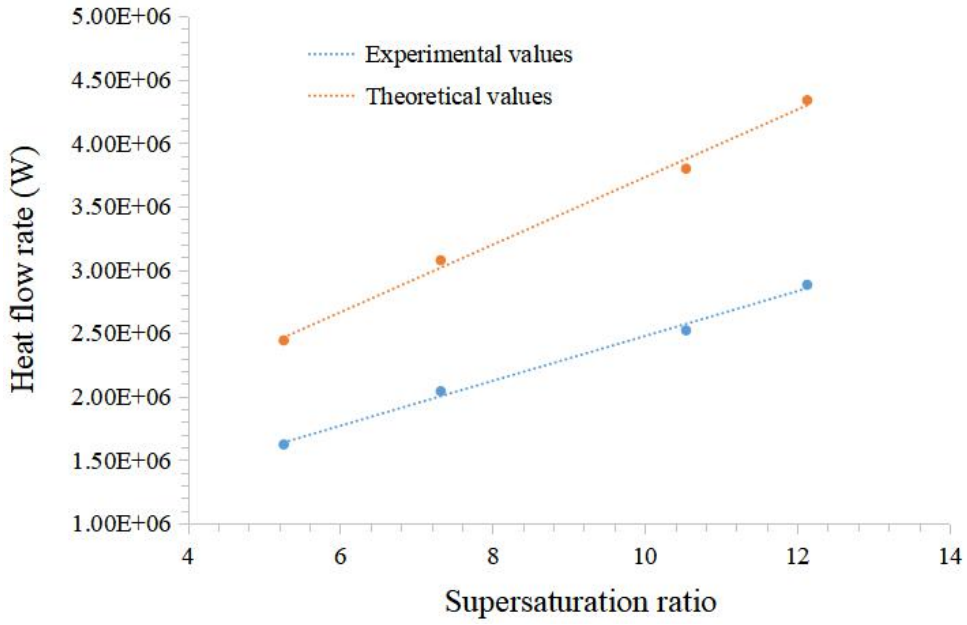

Fig. 20. Relationship between supersaturation ratio and heat flow rate.

4.5 Nucleation performance and big droplets speed of movement

To rule out the influence of topography (defects, roughness, etc.) on the nucleation density, we checked the nucleus distribution at the same location and temperature at two different times. As shown in Fig. 21, both pictures are captured right after the coalescence of a larger droplet, within the same video (65°C). Although there is a defect in the red circle on the surface, the nuclei distributed evenly overall. Therefore, the topography influence can be excluded. Interestingly, however, the difference of nucleation density is huge, up to 15-20 times, between the two images. Based on the presence of non-condensable gas, we think this observation is related to the presence of very large droplets in the vicinity (outside of the field of view) of the first case, which decrease the availability of vapor in the vapor diffusion layer surrounding them. The schematic on the influence of large droplets is shown in Fig. 22.

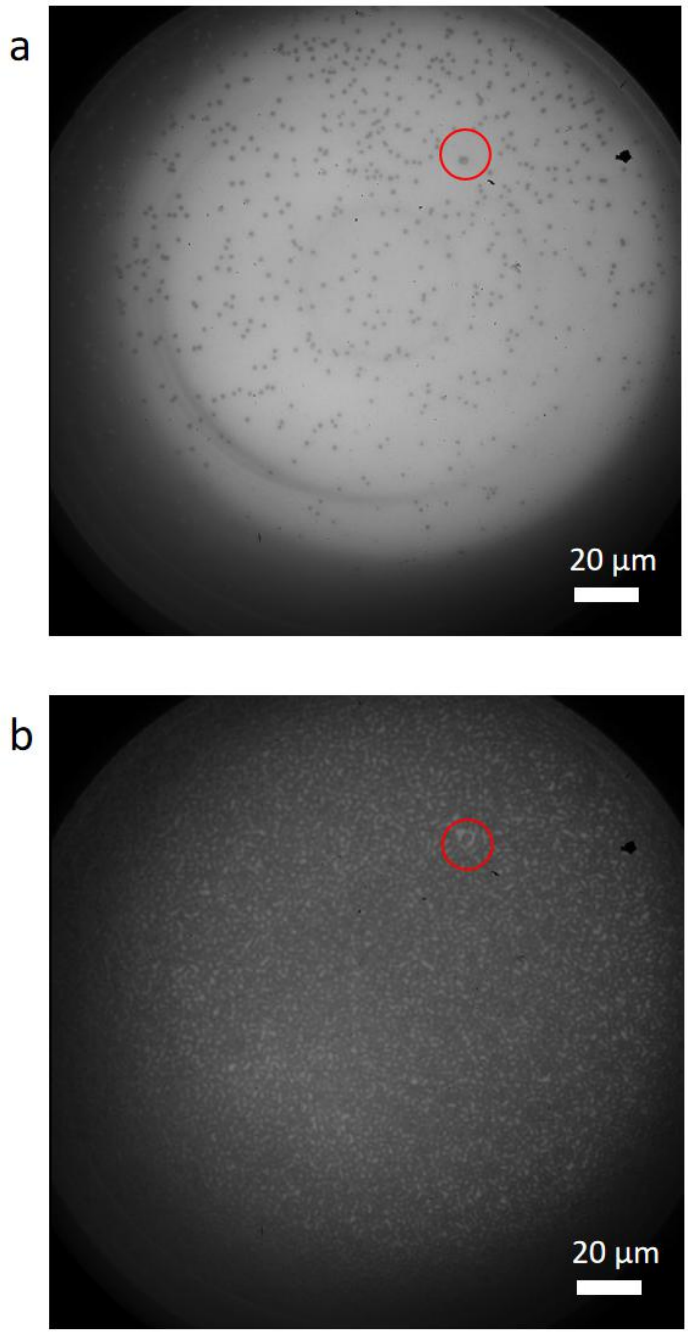

Fig. 21. Nucleation density at same location, but different time, at 65℃.

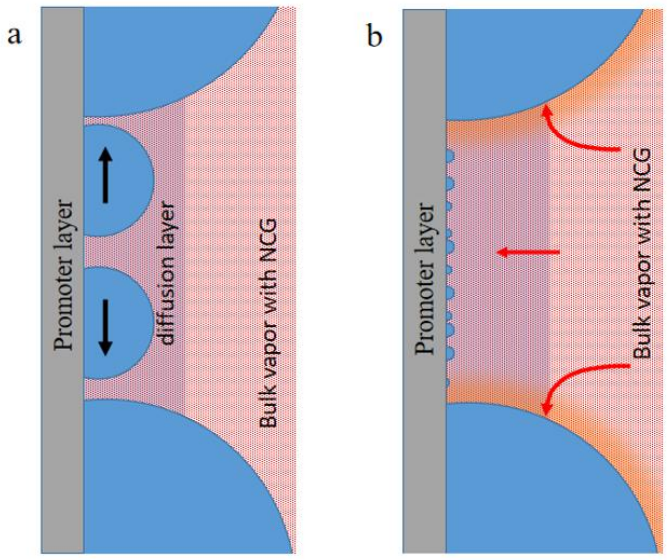

Fig. 22. Schematic of influence of large droplets.

In order to further explain this observation, we studied videos at different temperatures, and found that the speed of movement of big droplets has a strong effect on the nucleation density. As shown in Fig. 23, Fig. 23a to 23f are a series of pictures captured at 35℃ and same location. From Fig. 23a to 23c, a big droplet slowly moved from top to bottom. The nuclei behind it developed sparsely and the nucleation density is very low. At t=3.212 s, a big droplet coalesced with others and moved very quickly in the lower right corner. This action was finished within 0.006 seconds and left a large empty space for forming nuclei. It is easy to notice that in Fig. 23f the nucleation density is higher than before in Fig. 23b,c, despite the vapor temperature 35℃.

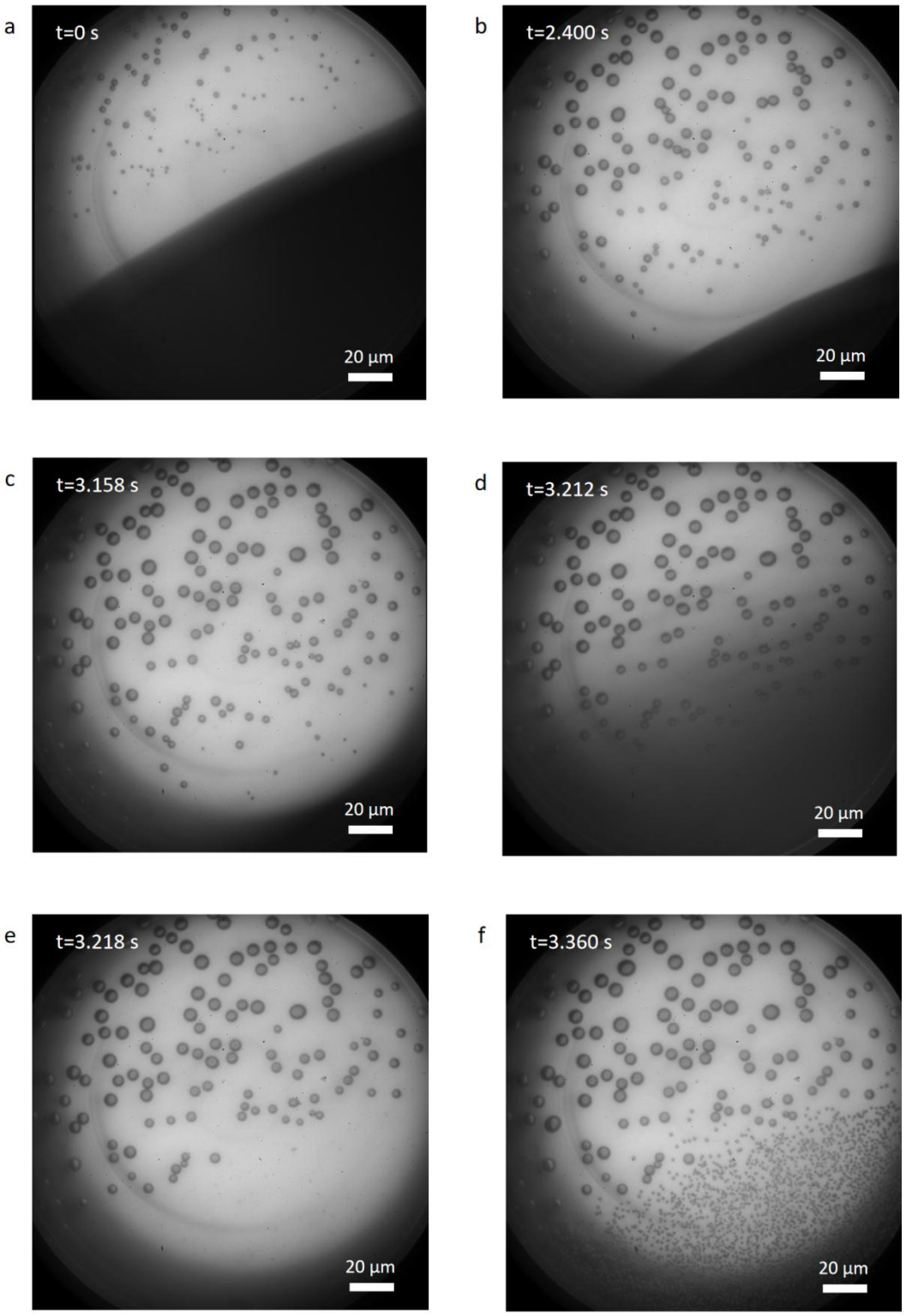

Fig. 23. Picture sequences of nucleation at 35℃.

Fig. 24 shows a similar phenomenon at 65℃. At the beginning, the big droplet coalesced with neighboring droplets, and moved fast within 0.1 seconds. In this process the nucleation generated densely. Then it moved slowly down after coalescing,

from Fig. 24b to 24c, and almost no new droplets formed. In Fig. 24d, the speed increased suddenly and slowed down at the end. During this time, the nuclei formed densely again. Finally, the droplet moved out of sight quickly and nucleation followed. We can see from Fig. 24e, there are two bands with sparse droplet density, which correspond to low droplet speeds. Therefore, if the coalescence between big droplets happens very fast, it can disturb the diffusion layer and enhance vapor transport to the subcooled surface. Therefore, it increases the nucleation density.

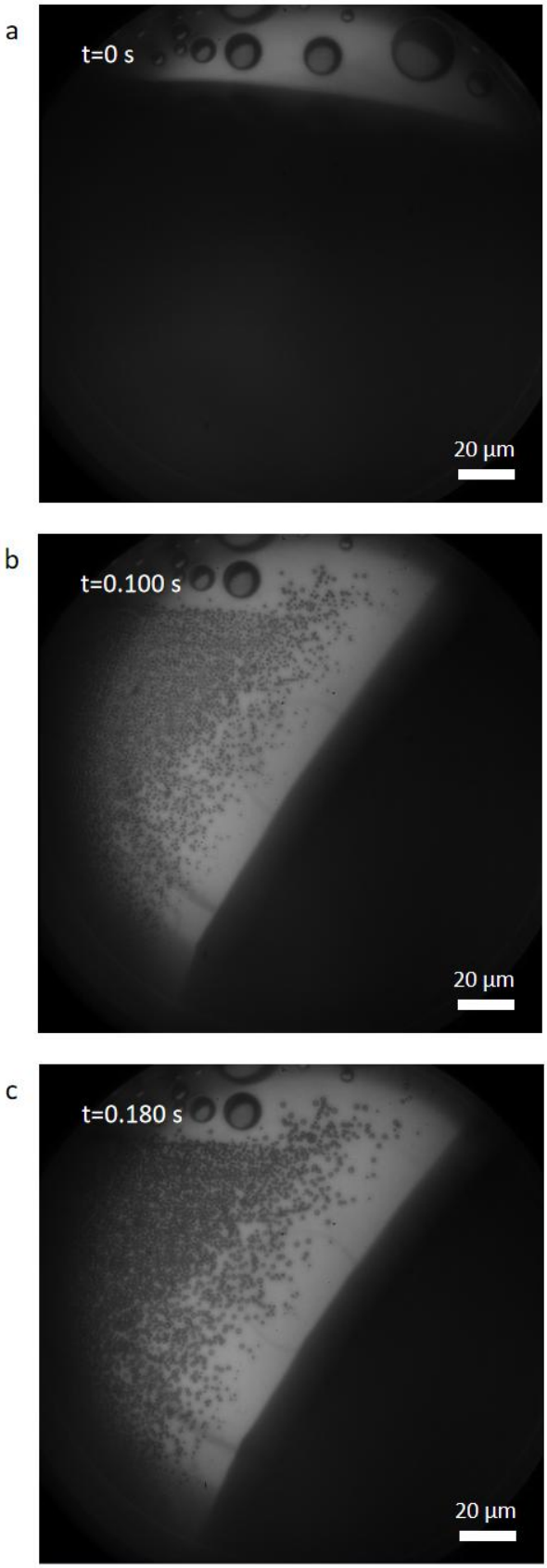

Fig. 24. Picture sequences of nucleation at 65℃ .

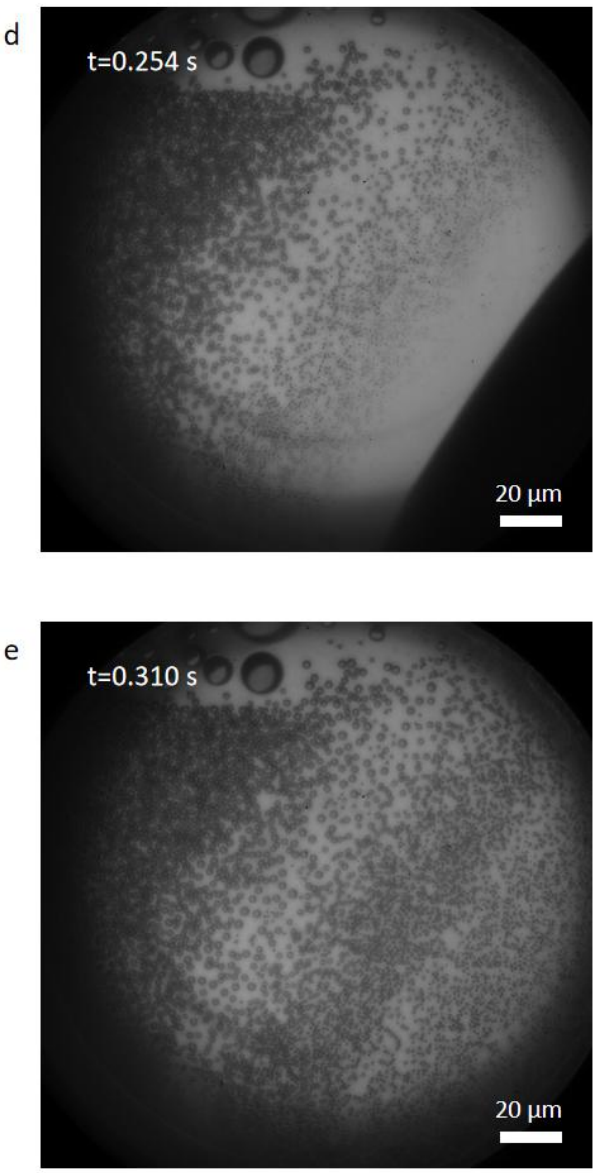

Fig. 24 (continued)

Based on the phenomenon, we briefly recap the process of disturbance, as shown in Fig. 25. When two big droplets coalesce, they will move to the centroid of the new droplets. This process is very quick and can happen in an instant. The movement strongly disturbs the diffusion layer and creates vortex that can make more vapor reach to the surface and condense on the surface, as shown in Fig. 25b. As the density of vapor increases, the nucleation density increases as well. Finally, the diffusion layer will revert within a short time after coalescing. Furthermore, Wen *et al* [58] used numerical calculation to analyze the vapor flow field near the surface when

disturbance happened. By simulation, they found a great unevenness of vapor flow behind the falling droplet. This uneven vapor flow field created a vortex, and the concentration gradient of water vapor in the diffusion boundary layer was broken by the vortex, thus the vapor transport from the vapor bulk to condensing surface was increased.

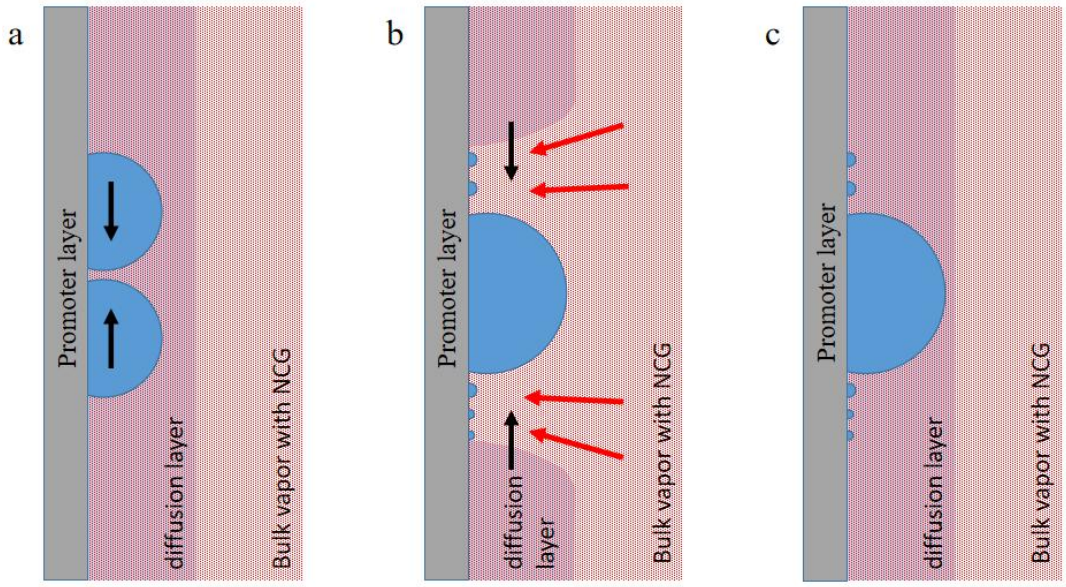

Fig. 25. Schematic of disturbance of diffusion layer by movement of big droplets.

Chapter 5: Conclusions

In summary, the growth pattern of nucleation density rate is exponential with the rise of supersaturation ratio. By analyzing, the growth rate of droplets, nucleation density and sweep frequency contribute to the change of nucleation density rate. The increase in nucleation density rate can also increase the heat transfer rate by emphasizing the heat transfer of small droplets. Compared with theoretical values, the nucleation density rate is restricted strongly by non-condensable gas, which can form a diffusion layer on the surface and increase the energy barrier for nucleation. However, a fast movement of big droplets can disturb the diffusion layer and increase the nucleation density rate by increasing the nucleation density.

References

[1]. E. Schmidt, W. Schurig, W. Sellschopp, Versuche über die Kondensation von Wasserdampf in Film-und Tropfenform, *Tech. Mech. Thermodyn*. 1 (1930) 53–63, http://dx.doi.org/10.1007/BF02641051.

[2]. Brunt, J. J. and Minken. (1958). The application of dropwise condensation to sea water evaporators. *Ind. Chem*., 34(5), 219– 224.

[3]. Eibling, J. A., & Hyatt, D. L. (1958). Methods of improving heat transfer in evaporators of small thermo-compression sea-water stills. *Chem. Engng Prog*, *54*(10), 84–86.

[4]. Garrett, D. E. (1958). Dropwise condensation in evaporators. *Br. Chem. Engng*, 3(9), 498–503.

[5]. Zhao, Q., Zhang, D., Zhu, X., Xu, D., Lin, Z., & Lin, J. (1990). Industrial application of dropwise condensation. *International Heat Transfer Conference Digital Library*.

[6]. Zhao, Q., Zhang, D., Zhu, X., Xu, D. and Lin, J. (1991a). The dropwise condenser design (in Chinese). *Natural J*., 14(3), 232–233.

[7]. Zhao, Q., Zhang, D., Li, S. P., Xu, D., Lin, J., Li, G., & Wang, G. (1991). Dropwise condensation of steam on ionplating surfaces. *Proc. of the Int. Conf. on Petroleum Refining and Petrochemical Processing*, *2*, 1049–1052.

[8]. Paxson, A. T., Yagüe, J. L., Gleason, K. K., & Varanasi, K. K. (2014). Stable dropwise condensation for enhancing heat transfer via the initiated chemical vapor deposition (iCVD) of grafted polymer films. *Advanced Materials*, *26*(3), 418–423.

[9]. S.A. Nada, H.F. Elattar, A. Fouda, Experimental study for hybrid humidification–dehumidification water desalination and air conditioning system, *Desalination* 363 (2015) 112–125, http://dx.doi.org/10.1016/j.desal.2015.01.032.

[10]. Seo, D., Lee, J., Lee, C., & Nam, Y. (2016). The effects of surface wettability on the fog and dew moisture harvesting performance on tubular surfaces. *Scientific reports*, *6*(1), 1–11.

[11]. Attinger, D., Frankiewicz, C., Betz, A. R., Schutzius, T. M., Ganguly, R., Das, A., Kim, C.-J., & Megaridis, C. M. (2014). Surface engineering for phase change heat transfer: A review. *MRS Energy & Sustainability*, *1*.

[12]. M. Jakob, *Heat transfer in evaporation and condensation*, Mech. Eng. 58 (1936) 729–739.

[13]. G. Tammann, W. Boehme, Die Zahl der Wassertröpfchen bei der Kondensation auf verschiedenen festen Stoffen, *Ann. Phys*. 414 (1) (1935) 77–80.

[14]. McCormick, J. L., & Baer, E. (1962). Dropwise condensation on horizontal surfaces. *Department of Chemistry and Chemical Engineering, University of Illinois*.

[15]. McCormick, J. L., & Baer, E. (1962). Dropwise condensation on horizontal surfaces. *Department of Chemistry and Chemical Engineering, University of Illinois*.

[16]. McCormick, J. L., & Westwater, J. W. (1966). Drop dynamics and heat transfer during dropwise condensation of water vapor on a horizontal surface. *Chemical Engineering Progress Symposium Series*, *62*(64), 120–134.

[17]. Umur, A., & Griffith, P. (1965). Mechanism of Dropwise Condensation. *Journal of Heat Transfer*, *87*(2), 275–282. https://doi.org/10.1115/1.3689090

[18]. Le Fevre, E. J., & Rose, J. W. (1966). A theory of heat transfer by dropwise condensation. *International Heat Transfer Conference Digital Library*.

[19]. McCormick, J. L., & Baer, E. (1963). On the mechanism of heat transfer in dropwise condensation. *Journal of Colloid Science*, *18*(3), 208–216.

[20]. Rose, J. W. (1967). On the mechanism of dropwise condensation. *International Journal of Heat and Mass Transfer*, *10*(6), 755–762. https://doi.org/10.1016/0017-9310(67)90135-4

[21]. Gose, E. E., Mucciardi, A. N., & Baer, E. (1967). Model for dropwise condensation on randomly distributed sites. *International Journal of Heat and Mass Transfer*, *10*(1), 15–22.

[22]. Hurst, C. J., *Transient Droplet Growth During Dropwise Condensation*, Ph.D. Thesis, Penn. State University (1966).

[23]. Glicksman, L. R. , *An Analytical Study of Dropwise Condensation*, To be published in Int. J. Heat Mass Transfer .

[24]. Mikic, B. B. (1969). On mechanism of dropwise condensation. *International Journal of Heat and Mass Transfer*, *12*(10), 1311–1323. https://doi.org/10.1016/0017-9310(69)90174-4

[25]. Graham, C., & Griffith, P. (1973). Drop size distributions and heat transfer in dropwise condensation. *International Journal of Heat and Mass Transfer*, *16*(2), 337–346. https://doi.org/10.1016/0017-9310(73)90062-8

[26]. Wen, H. W., & Jer, R. M. (1976). On the heat transfer in dropwise condensation. *The chemical engineering journal*, *12*(3), 225–231.

[27] Abu-Orabi, M. (1998). Modeling of heat transfer in dropwise condensation. *International journal of heat and mass transfer*, *41*(1), 81–87.

[28] Wu, Y.-T., Yang, C.-X., & Yuan, X.-G. (2001). Drop distributions and numerical simulation of dropwise condensation heat transfer. *International Journal of Heat and Mass Transfer*, *44*(23), 4455–4464.

[29]. Kim, S., & Kim, K. J. (2011). Dropwise condensation modeling suitable for superhydrophobic surfaces. *Journal of heat transfer*, *133*(8).

[30]. Liu, X., & Cheng, P. (2015). Dropwise condensation theory revisited: Part I. Droplet nucleation radius. *International Journal of Heat and Mass Transfer*, *83*, 833–841. https://doi.org/10.1016/j.ijheatmasstransfer.2014.11.009

[31]. Liu, X., & Cheng, P. (2015). Dropwise condensation theory revisited Part II. Droplet nucleation density and condensation heat flux. *International Journal of Heat and Mass Transfer*, *83*, 842–849. https://doi.org/10.1016/j.ijheatmass transfer.2014.11.008

[32]. Rose, J. W. (2002). Dropwise condensation theory and experiment: A review. *Proceedings of the Institution of Mechanical Engineers, Part A: Journal of Power and Energy*, *216*(2), 115–128.

[33]. Tanner, D. W., Potter, C. J., Pope, D., & West, D. (1965). Heat transfer in dropwise condensation—Part I The effects of heat flux, steam velocity and non-condensable gas concentration. *International Journal of Heat and Mass Transfer*, *8*(3), 419–426.

[34]. Tanner, D. W., Pope, D., Potter, C. J., & West, D. (1968). Heat transfer in dropwise condensation at low steam pressures in the absence and presence of non-condensable gas. *International Journal of Heat and Mass Transfer*, *11*(2), 181–190.

[35]. B.J. Chung, S. Kim, M.C. Kim, M. Ahmadinejad, Experimental comparison of filmwise and dropwise condensation of steam on vertical flat plates with the presence of air, *Int. Commun. Heat Mass Transfer 31* (8) (2004) 1067–1074.

[36]. Ma, X.-H., Zhou, X.-D., Lan, Z., Yi-Ming, L. I., & Zhang, Y. (2008). Condensation heat transfer enhancement in the presence of non-condensable gas using the interfacial effect of dropwise condensation. *International Journal of Heat and Mass Transfer*, *51*(7–8), 1728–1737.

[37]. Huang, J., Zhang, J., & Wang, L. (2015). Review of vapor condensation heat and mass transfer in the presence of non-condensable gas. *Applied thermal engineering*, *89*, 469–484.

[38]. Zheng, S., Eimann, F., Philipp, C., Fieback, T., & Gross, U. (2018). Modeling of heat and mass transfer for dropwise condensation of moist air and the

experimental validation. *International Journal of Heat and Mass Transfer*, *120*, 879–894.

[39]. Quan, X., Yang, L., & Cheng, P. (2014). Effects of electric fields on onset of dropwise condensation based on Gibbs free energy and availability analyses. *International Communications in Heat and Mass Transfer*, *58*, 105–110.

[40]. S. Khandekar, K. Muralidhar, *Modeling dropwise condensation, in: Dropwise Condensation on Inclined Textured Surfaces*, Springer, 2014, pp. 17–72.

[41]. Dong, L., Cheng, P., & Quan, X. (2012). Availability analyses for heterogeneous nucleation under steady heating in pool boiling. *International communications in heat and mass transfer*, *39*(6), 776–780.

[42]. Le Fevre, E. J., & Rose, J. W. (1966). A theory of heat transfer by dropwise condensation. *International Heat Transfer Conference Digital Library*.

[43]. Rose, J. W. (1976). Further aspects of dropwise condensation theory. *International Journal of Heat and Mass Transfer*, *19*(12), 1363–1370.

[44]. Cha, H., Wu, A., Kim, M.-K., Saigusa, K., Liu, A., & Miljkovic, N. (2017). Nanoscale-agglomerate-mediated heterogeneous nucleation. *Nano letters*, *17*(12), 7544–7551.

[45]. Mu, C., Pang, J., Lu, Q., & Liu, T. (2008). Effects of surface topography of material on nucleation site density of dropwise condensation. *Chemical engineering science*, *63*(4), 874–880.

[46]. Enright, R., Miljkovic, N., Al-Obeidi, A., Thompson, C. V., & Wang, E. N. (2012). Condensation on superhydrophobic surfaces: The role of local energy barriers and structure length scale. *Langmuir*, *28*(40), 14424–14432.

[47]. Weisensee, P. B., Wang, Y., Qian, H., Schultz, D., King, W. P., & Miljkovic, N. (2017). Condensate droplet size distribution on lubricant-infused surfaces. *International Journal of Heat and Mass Transfer*, *109*, 187–199. https://doi.org/10.1016/j.ijheatmasstransfer.2017.01.119

[48]. Neumann, A. W., Abdelmessih, A. H., & Hameed, A. (1978). The role of contact angles and contact angle hysteresis in dropwise condensation heat transfer. *International Journal of Heat and Mass Transfer*, *21*(7), 947–953.

[49]. Medici, M.-G., Mongruel, A., Royon, L., & Beysens, D. (2014). Edge effects on water droplet condensation. *Physical Review E*, *90*(6), 062403. https://doi.org/10.1103/PhysRevE.90.062403

[50]. Wood, J., & Sharma, R. (1994). Preparation of a robust hydrophobic monolayer on mica. *Langmuir*, *10*(7), 2307–2310.

[51]. Parker, J. L., Cho, D. L., & Claesson, P. M. (1989). Plasma modification of mica: Forces between fluorocarbon surfaces in water and a nonpolar liquid. *The Journal of Physical Chemistry*, *93*(16), 6121–6125.

[52]. Endo, K., Shinoda, K., & Tatsumi, T. (1999). Plasma deposition of low-dielectric-constant fluorinated amorphous carbon. *Journal of applied physics*, *86*(5), 2739–2745.

[53]. Metya, A., Ghose, D., & Ray, N. R. (2014). Development of hydrophobicity of mica surfaces by ion beam sputtering. *Applied Surface Science*, *293*, 18–23. https://doi.org/10.1016/j.apsusc.2013.11.163

[54]. Sauthier, G., Segura, J. J., Fraxedas, J., & Verdaguer, A. (2014). Hydrophobic coating of mica by stearic acid vapor deposition. *Colloids and Surfaces A: Physicochemical and Engineering Aspects*, *443*, 331–337. https://doi.org/10.1016/j.colsurfa.2013.11.031

[55]. *Super-Hydrophobic Coatings Prepared by RF Magnetron Sputtering of PTFE - Drábik—2010—Plasma Processes and Polymers—Wiley Online Library*. (n.d.). Retrieved April 16, 2020, from https://onlinelibrary.wiley.com/doi/full/10.1002/ppap.200900164?casa_token=aE5PyMsgtaoAAAAA%3AlU-KBU1RgFksEbvqvnBoAyFMQ_NuRRIi5riUDPzIY1rHbKs0o_pKowI04QpqR7DFUjQUXCFb-lgoXg

[56]. Carey, V. P. (2020). *Liquid-Vapor Phase-Change Phenomena: An Introduction to the Thermophysics of Vaporization and Condensation Processes in Heat Transfer Equipment, Third Edition*. CRC Press.

[57]. *Heterogeneous nucleation capability of conical microstructures for water droplets—RSC Advances (RSC Publishing) DOI:10.1039/C4RA12352B*. (n.d.). Retrieved April 16, 2020, from https://pubs.rsc.org/en/content/articlehtml/2014/ra/c4ra12352b

[58] Wen, R., Zhou, X., Peng, B., Lan, Z., Yang, R., & Ma, X. (2019). Falling-droplet-enhanced filmwise condensation in the presence of non-condensable gas. *International Journal of Heat and Mass Transfer*, *140*, 173–186. https://doi.org/10.1016/j.ijheatmasstransfer.2019.05.110